Chapter 3
Air and Abrasive Acceleration

3.1 Properties of Compressed Air

Air is a colourless, odourless and tasteless gas mixture. It consists of many gases, but primarily of oxygen (21%) and nitrogen (78%). Air is always more or less contaminated with solid particles, for example, dust, sand, soot and salt crystals. Typical properties of air are listed in Table 3.1. If air is considered to be an ideal gas, its behaviour can be described based on the general law of state:

$$p \cdot \upsilon_S = R_i \cdot T \tag{3.1}$$

where p is the static air pressure, υ_S is the specific volume of the gas, R_i is the individual gas constant and T is the absolute temperature. It can be distinguished between three pressure levels, which are illustrated in Fig. 3.1. The relationships between these pressure levels are as follows:

$$p = p_0 + p_G \tag{3.2}$$

The parameter p is the absolute pressure, the parameter p_G is the gauge pressure usually read by the pressure gages in the blast cleaning pressure systems, and the parameter p_0 is the atmospheric pressure. The atmospheric pressure is a function of altitude. It is important not to confuse the absolute pressure and the gauge pressure. For theoretical calculations, the absolute pressure must be used.

The parameter R_i in (3.1) is the individual gas constant, which is the energy delivered by a mass of 1 kg of air if its temperature is increased by +1°C (K) at constant pressure. Its value for air is provided in Table 3.1. The individual gas constant is the difference between isobaric heat capacity and isochoric heat capacity of the gas:

$$R_i = c_P - c_V \tag{3.3}$$

The ratio between isobaric heat capacity and isochoric heat capacity is the isentropic exponent of the gas:

$$\kappa = \frac{c_P}{c_V} \tag{3.4}$$

Table 3.1 Properties of air

Parameter	Symbol	Unit	Value
Density[a]	ρ_A	kg/m^3	1.225
Dynamic viscosity[a]	η_0	Ns/m^2	1.72×10^{-5}
Isobaric specific heat capacity[b]	c_P	Nm/(kg K)	1,004
Isochoric specific heat capacity[b]	c_V	Nm/(kg K)	717
Gas constant	R_i	Nm/(kg K)	287
Adiabatic exponent	κ	–	1.4
Critical pressure ratio	β	–	0.528
Kinematic viscosity	ν_A	m^2/s	1.82×10^{-5}
Specific evaporation heat	q_V	Nm/kg	1.97×10^{-5}
Speed of sound[a]	c	m/s	331
Sutherland parameter	C_S	K	113

[a]Thermodynamic standard (Table 3.2: $\vartheta = 0°C$, $p = 0.101325$ MPa)
[b]For $T = 273$ K

Values for the heat capacities and for the isentropic exponent of air can be found in Table 3.1. The absolute temperature is given as follows:

$$T = \vartheta + 273.2 \tag{3.5}$$

Its physical unit is K. The parameter ϑ is the temperature at the Celsius scale (°C). With $\upsilon_S = 1/\rho_A$, (3.1) reads as follows:

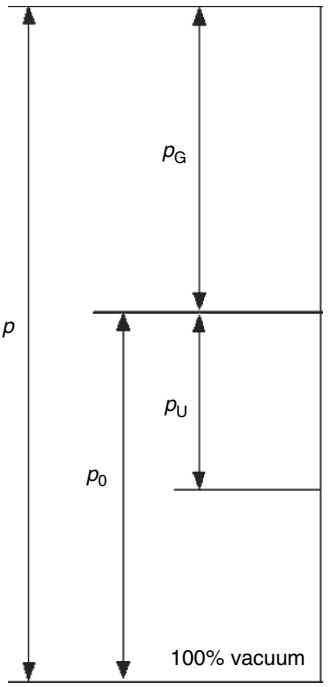

Fig. 3.1 Pressure levels

$$\frac{p}{\rho_A} = R_i \cdot T \tag{3.6}$$

This equation suggests that air density depends on pressure and temperature. These relationships are displayed in Fig. 3.2. For $T = 288.2\,\mathrm{K}$ ($\vartheta = 15^\circ\mathrm{C}$) and $p = p_0 = 0.101325\,\mathrm{MPa}$, the density of air is $\rho_A = 1.225\,\mathrm{kg/m^3}$ according to (3.6).

The volume of air depends on its state. The following four standards can be distinguished for the state of air:

- physical normal condition (DIN 1343, 1990);
- industry standard condition (ISO 1217, 1996);
- environmental condition;
- operating condition.

These standards are defined in Table 3.2. It can be seen that the physical normal condition and the industry standard condition both apply to dry air only with a relative humidity of 0%. For wet air, corrective factors must be considered (see DIN 1945-1).

The dynamic viscosity of air is independent of pressure for most technical applications, but it depends on temperature according to the following relationship (Albring, 1970):

$$\eta_A = \eta_0 \cdot \left(\frac{T}{T_0}\right)^{1/2} \cdot \frac{1 + (C_S/T_0)}{1 + (C_S/T)} \tag{3.7}$$

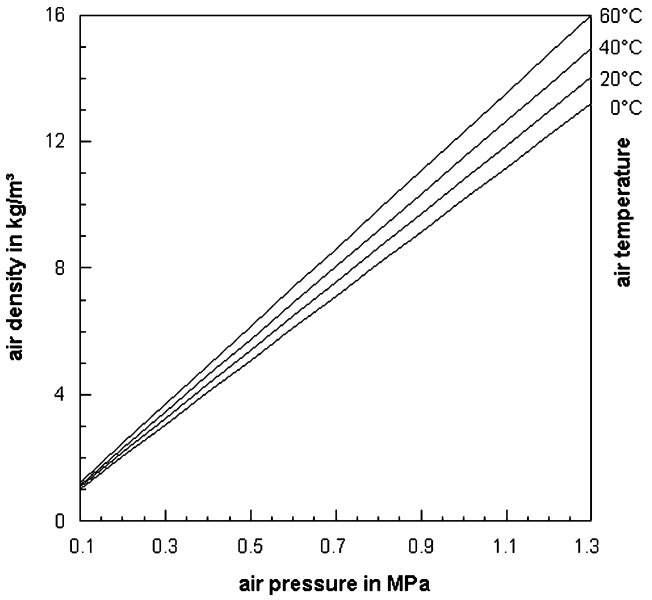

Fig. 3.2 Relationship between air pressure, air temperature and air density

Table 3.2 Conditions of state for air (DIN 1343, ISO 1217)

State	Temperature	Air pressure	Relative humidity	Air density
Physical standard (Normative standard)	0°C = 273.15 K	1.01325 bar = 0.101325 MPa	0%	1.294 kg/m^3
Industry standard	20°C = 293.15 K	1.0 bar = 0.1 MPa	0%	–
Environmental condition	Environmental temperature	Environmental pressure	Environmental humidity	Variable
Operating condition	Operating temperature	Operating pressure	Variable	Variable

The Sutherland parameter C_S for air is listed in Table 3.1. Results of (3.7) are plotted in Fig. 3.3, and it can be seen that dynamic viscosity rises almost linearly with an increase in temperature (in contrast to water, where dynamic viscosity decreases with an increase in temperature). The kinematic viscosity of air depends on pressure, and the relationship is as follows:

$$\nu_A = \frac{\eta_A}{\rho_A} \tag{3.8}$$

with $\rho_A = f(p, T)$.

The speed of sound in air is a function of the gas properties and absolute temperature:

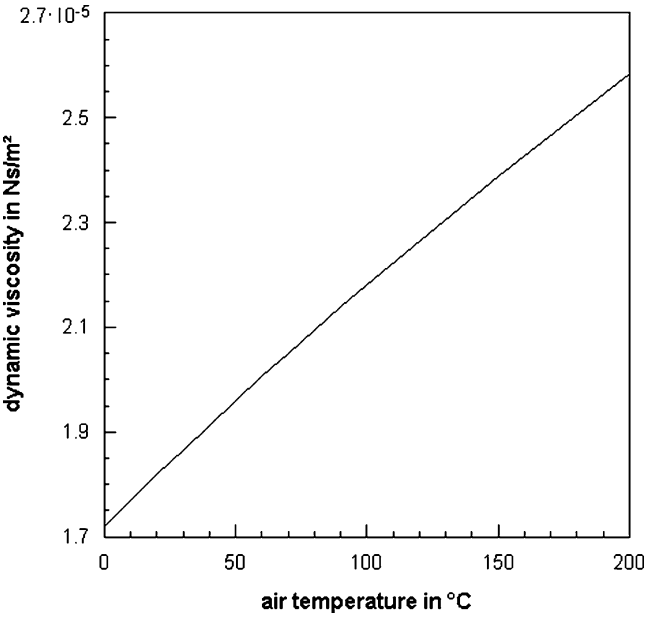

Fig. 3.3 Relationship between air temperature and dynamic viscosity of air

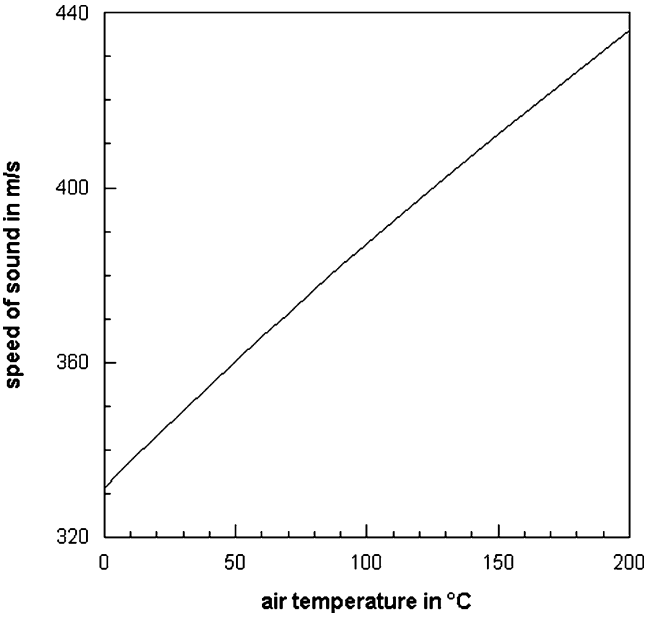

Fig. 3.4 Relationship between air temperature and speed of sound in air

$$c = (\kappa \cdot R_i \cdot T)^{1/2} \tag{3.9}$$

Results of (3.9) for different air temperatures are plotted in Fig. 3.4. The ratio between the actual local flow velocity and the speed of sound is the Mach number, which is defined as follows:

$$Ma = \frac{v_F}{c} \tag{3.10}$$

For $Ma < 1$, the flow is subsonic, and for $Ma > 1$, the flow is supersonic. For $Ma = 1$, the flow is sonic.

3.2 Air Flow in Nozzles

3.2.1 Air Mass Flow Rate Through Nozzles

Because air is a compressible medium, volumetric flow rate is not a constant value, and mass flow rate conversion counts for any calculation. The theoretical mass flow rate of air through a nozzle is given by the following equation (Bohl, 1989):

$$\dot{m}_{Ath} = \frac{\pi}{4} \cdot d_N^2 \cdot \left(2 \cdot \rho_A \cdot p\right)^{1/2} \cdot \underbrace{\left\{ \frac{\kappa}{\kappa - 1} \cdot \left[\left(\frac{p_0}{p} \right)^{\frac{2}{\kappa}} - \left(\frac{p_0}{p} \right)^{\frac{\kappa+1}{\kappa}} \right] \right\}^{1/2}}_{\text{outflow function } \Psi} \tag{3.11}$$

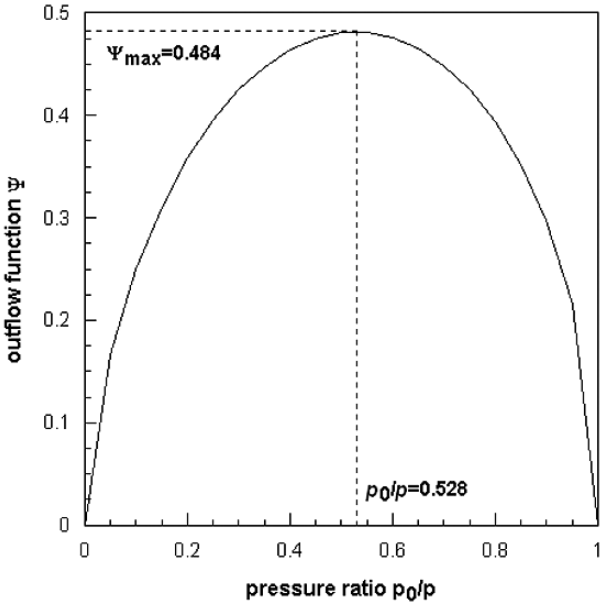

Fig. 3.5 Outflow function $\Psi = \mathrm{f}(p_0/p)$ for air

The outflow function $\Psi = \mathrm{f}(p_0/p)$ is plotted in Fig. 3.5. It is a parabolic function with a typical maximum value at a critical pressure ratio p_0/p. This critical pressure ratio is often referred to as *Laval pressure ratio*. It can be estimated as follows:

$$\left(\frac{\mathrm{p_0}}{\mathrm{p}}\right)_{\mathrm{crit}} = \left(\frac{2}{\kappa+1}\right)^{\frac{\kappa}{\kappa-1}} \tag{3.12a}$$

With $\kappa = 1.4$ for air, (3.12a) delivers the following value for the Laval pressure ratio:

$$\left(\frac{\mathrm{p_0}}{\mathrm{p}}\right)_{\mathrm{crit}} = 0.528 \tag{3.12b}$$

The corresponding value for the outflow function is $\psi_{\max}(0.528) = 0.484$. The graph plotted in Fig. 3.5 does not describe reality. In reality, air mass flow rate does not drop for pressure ratios < 0.528. The air mass flow rate rather follows the horizontal dotted line for $\psi_{\max} = 0.484$. Equation (3.11) can, therefore, be simplified for the condition $p_0/p < 0.528$ (respectively $p > 0.19\,\mathrm{MPa}$ for $p_0 = 0.1\,\mathrm{MPa}$):

$$\dot{\mathrm{m}}_{\mathrm{Ath}} = \frac{\pi}{4} \cdot \mathrm{d_N^2} \cdot \left(2 \cdot \rho_{\mathrm{A}} \cdot \mathrm{p}\right)^{1/2} \cdot 0.484 \tag{3.13}$$

Equation (3.13) delivers the theoretical mass flow rate. The real mass flow rate includes a nozzle exit parameter:

Table 3.3 Nozzle exit coefficient α_N (Schwate, 1986)

Nozzle geometry	α_N-value
Sharp-edged opening	0.6
Opening with $l_N = 1.5 \cdot d_N$	0.8
Conical entry opening with rounded edges	0.9
Very smooth surface; rounded edges with radius $= 0.5 \cdot d_N$	0.95

$$\dot{m}_A = \alpha_N \cdot \frac{\pi \cdot 0.484}{4} \cdot d_N^2 \cdot \left(2 \cdot \rho_A \cdot p\right)^{1/2} \tag{3.14}$$

The values for the nozzle exit coefficient α_N depend on nozzle geometry. Some values are listed in Table 3.3. Calculated theoretical air mass flow rates are plotted in Fig. 3.6. It can be seen that the mass flow rate linearly increases with an increase in nozzle pressure.

3.2.2 Volumetric Air Flow Rate

The volumetric air flow rate can be calculated as follows:

$$\dot{Q}_A = \frac{\dot{m}_A}{\rho_A} \tag{3.15}$$

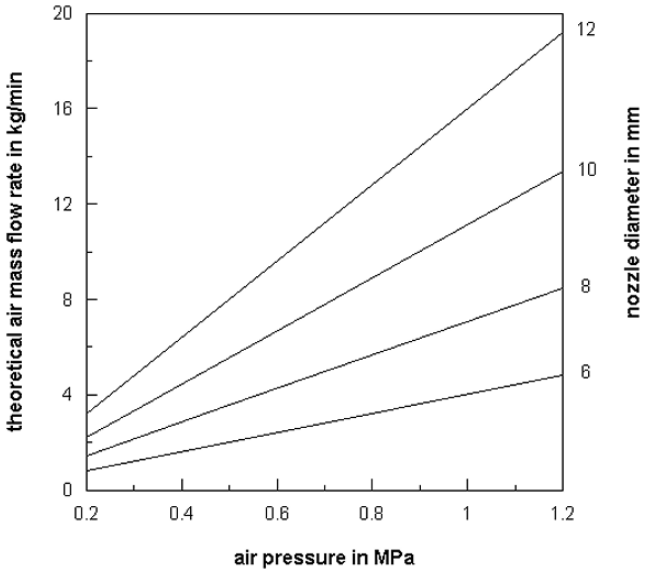

Fig. 3.6 Theoretical mass flow rates for a blast cleaning nozzle as functions of pressure and nozzle diameter (air temperature: 20 °C)

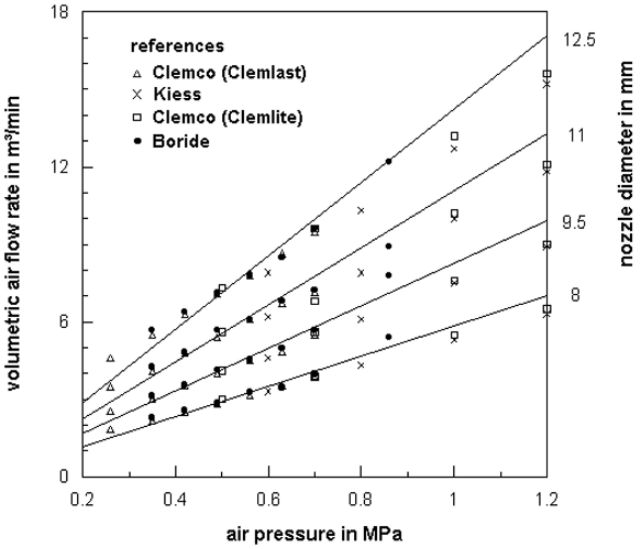

Fig. 3.7 Theoretical volumetric flow rates for a compressor (for an ambient air temperature of $\vartheta = 20°\mathrm{C}$) and recommended values from equipment manufacturers

The density is given through (3.6). If the volumetric flow rate, which must be delivered by a compressor, is requested, the density ρ_A for the environmental conditions (see Table 3.2) must be inserted in (3.15). Because air density depends on temperature, the ambient air temperature in the vicinity of a compressor may affect the volumetric air rate. A change in ambient air temperature of $\Delta T = 10\,K$ ($\Delta\vartheta = 10\,°\mathrm{C}$), however, leads to a 3%-change in the volumetric air flow rate.

Results of (3.14) and (3.15) for typical parameter configurations are plotted in Fig. 3.7 together with recommendations issued by equipment manufacturers. The deviations between calculation and recommendation cannot be neglected for nozzle pressures higher than $p = 0.9\,\mathrm{MPa}$. Results obtained with (3.14) and (3.15) correspond very well with results of measurements reported by Nettmann (1936). For $p = 0.5\,\mathrm{MPa}$ (gauge pressure) and $d_N = 10\,\mathrm{mm}$, this author reported a value of $\dot{Q}_A = 5.65\,\mathrm{m^3/min}$. The calculation (based on industry standard, $\vartheta = 20\,°\mathrm{C}$) delivers $\dot{Q}_A = 5.63\,\mathrm{m^3/min}$. Nettmann (1936) was probably the first who published engineering nomograms for the assessment of compressor volumetric air flow rate and of compressor power rating for varying gauge pressures and nozzle diameters. Equations (3.14) and (3.15) can be utilised to calculate nozzle working lines. Working lines for three different nozzles are plotted in Fig. 4.3.

If abrasive material is added to the air flow, it occupies part of the nozzle volume and displaces part of the air. This issue was in detail investigated experimentally by Adlassing (1960), Bae et al. (2007), Lukschandel (1973), Uferer (1992) and Plaster (1973); and theoretically by Fokke (1999). Fokke (1999) found that the abrasive particle volume fraction in the nozzle flow depended on abrasive mass flow rate, and it had values between $F_P = 0.01$ (1 vol.%) and 0.04 (4 vol.%).

Uferer (1992) derived a critical abrasive volume fraction for blast cleaning processes, and he suggested that the value of $F_P = 0.12$ (12 vol.%) should not be exceeded in order to guarantee a stable blast cleaning process.

Due to the dislocation effect, the air flow rate through a nozzle reduces if abrasive material is added to the flow, and a modified relationship reads as follows:

$$\dot{Q}_{A(P)} = \Phi_P \cdot \dot{Q}_A \tag{3.16}$$

The reduction parameter has typical values between $\Phi_P = 0.7$ and 0.9; it depends mainly on abrasive mass flow rate (Adlassing, 1960; Lukschandel, 1973; Plaster, 1973; Uferer, 1992; Bae et al., 2007). Fokke (1999) found that particle size had a very small influence on the air mass flow rate if rather high air pressures were applied.

Uferer (1992) recommended the following relationship for the estimation of the reduction parameter:

$$\Phi_P = \frac{1}{\left(1 + \frac{V_P}{V_A} \cdot \frac{\dot{m}_P}{\dot{m}_A}\right)^{1/2}} \tag{3.17}$$

For typical blast cleaning parameters ($\dot{m}_P/\dot{m}_A = 2,\ v_P/v_A = 0.3$), this equation delivers $\Phi_P = 0.79$, which is in agreement with the reported experimental results. Values estimated by Uferer (1992) are listed in Table 3.4. It can be seen that the value of the reduction parameter depended on abrasive type, nozzle geometry and mass flow ratio abrasive/air. For the range $R_m = 1.5$ to 3, which is recommended for blast cleaning processes, the values for the reduction parameter were between $\Phi_P = 0.75$ and 0.85.

Bae et al. (2007) and Remmelts (1968) performed measurements of volumetric air flow rates as a function of abrasive mass flow rate. Their results, partly plotted in Fig. 3.11, can be fitted with the following exponential regression:

$$\Phi_{P(Laval)} = \frac{\dot{Q}_{A(P)}}{\dot{Q}_A} = 0.98^{\dot{m}_P} \tag{3.18a}$$

Table 3.4 Reduction parameter values for different blast cleaning conditions (Uferer, 1992)

Abrasive type	Nozzle geometry	Mass flow ratio abrasive/air	Φ_P
Slag and quartz sand	Cylindrical	< 1.5	0.8
		1.5–3	0.75
	Convergent-divergent (Laval)	< 1.5	0.9
		1.5–3	0.85
Cut steel wire	Cylindrical	< 1.5	0.8
		1.5–3.5	0.75
		3.5–5.5	0.7
		> 5.5	0.6

The abrasive mass flow rate must be inserted in kg/min. The coefficient of regression is as high as 0.95 for all fits. It can be seen that $\Phi_P = 1$ for $\dot{m}_P = 0$. For a typical abrasive mass flow rate of $\dot{m}_P = 10$ kg/min, the equation delivers $\Phi_P = 0.82$, which corresponds well with the values cited earlier. The regression is valid for Laval nozzles fed with steel grit. The basic number 0.98 in (3.18a) is independent of the dimensions of the nozzles (d_N, l_N), and it can be assumed to be typical for Laval nozzles. However, the basic number may change if other abrasive materials than steel grit are utilised.

Results of measurements of volumetric flow rates performed by some authors are presented in Figs. 3.8 and Fig. 3.9. The results provided in Fig. 3.8 demonstrate the effects of different abrasive types on the volumetric air flow rate. The addition of chilled iron was more critical to the volumetric air flow rate compared with the addition of the non-ferrous abrasive material. The results plotted in Fig. 3.9 showed that air volumetric flow rate depended on abrasive type, nozzle type and air pressure, if abrasive material was added. Interestingly, the effect of the abrasive material type was only marginal for small nozzle diameters. This effect was also reported by Adlassing (1960). The reduction in air flow rate was more severe if a Laval nozzle was utilised instead of a standard nozzle. Laval nozzles consumed approximately 10% more air volume than conventional cylindrical nozzles, if abrasives (quartz, SiC, corundum and steel grit) were added (Lukschandel, 1973). This result agrees with measurements provided in Table 3.4. Based on these results, the following very preliminary approach can be made:

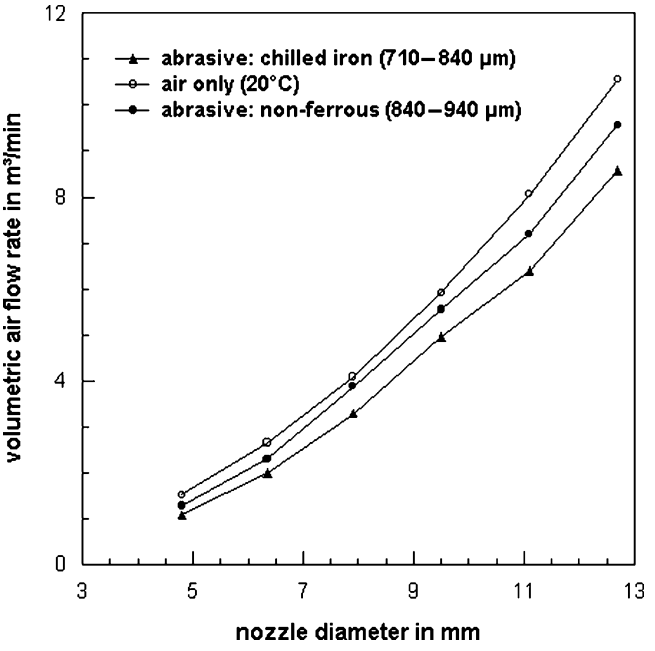

Fig. 3.8 Effect of abrasive type on volumetric air flow rate (Plaster, 1973)

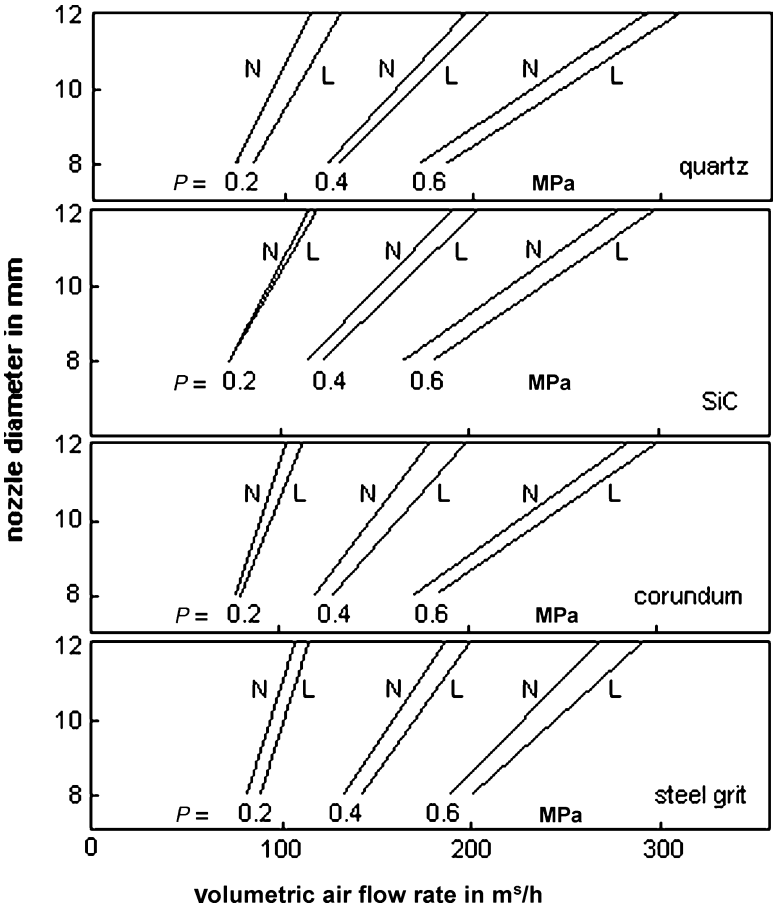

Fig. 3.9 Effects of air pressure, nozzle diameter, nozzle geometry and abrasive type on volumetric air flow rate (Lukschandel, 1973). "N" – cylindrical nozzle; "L" – convergent–divergent (Laval) nozzle

$$\Phi_{P(\text{cylinder})} = 0.9 \cdot \Phi_{P(\text{Laval})} \tag{3.18b}$$

More experimental evidence is provided in Figs. 3.10 and 3.11. Figure 3.10 illustrates the effect of nozzle layout on the air volume flow, if abrasive material (crushed cast iron) was added. The deviation in air volume flow rate was about 10%. The effects of varying nozzle geometries on the volumetric air flow rates were further investigated by Bae et al. (2007). Some of their results are displayed in Fig. 3.11. The effect of nozzle geometry parameters is much more pronounced compared with the results plotted in Fig. 3.10. The graphs also illustrate the effects of abrasive mass flow rate on the volumetric air flow rate. The more the abrasive material added, the lesser the air volume flow through the nozzle. The curves ran parallel to each

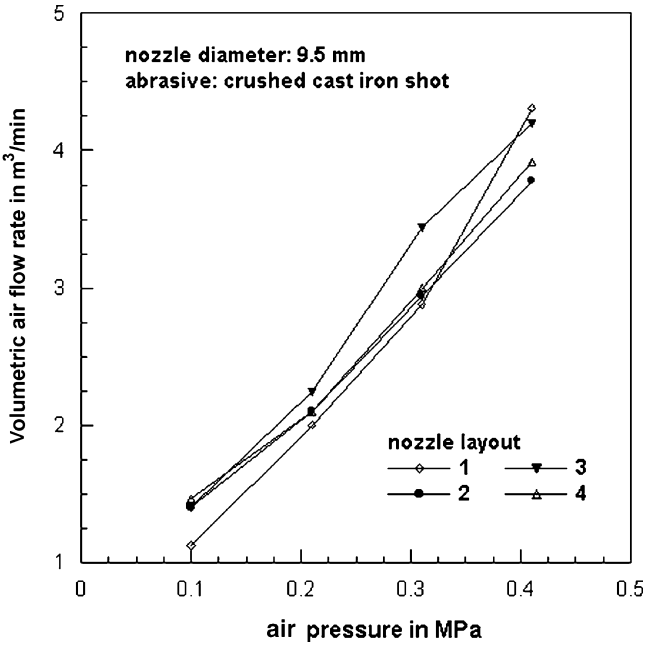

Fig. 3.10 Effects of nozzle geometry on volumetric air flow rate (Plaster, 1973); abrasive type: crushed chilled cast iron shot; $d_N = 9.5$ mm. Nozzle layout: "1" – convergent–divergent; "2" – bell-mouthed + convergent; "3" – bell-mouthed + divergent; "4": bell-mouthed + convergent–divergent

other; thus, the general trend was almost independent of the nozzle geometry. These relationships are expressed through (3.18a).

3.2.3 Air Exit Flow Velocity in Nozzles

For an isotropic flow (no heat is added or taken and no friction), the velocity of an air jet exiting a pressurised air reservoir through a small opening can be expressed as the enthalpy difference between vessel and environment as follows:

$$v_A = (2 \cdot \Delta h_A)^{1/2} \tag{3.19}$$

After some treatment, the velocity of air flow at the exit of a nozzle can be calculated with the following relationship (Kalide, 1990):

$$v_A = \left(2 \cdot \frac{\kappa}{\kappa - 1} \cdot \frac{p}{\rho_A} \cdot \left[1 - \left(\frac{p_0}{p}\right)^{\frac{\kappa-1}{\kappa}}\right]\right)^{1/2} \tag{3.20}$$

As an example, if compressed air at a temperature of $\vartheta = 27°C$ ($T = 300$ K) and at a pressure of $p = 0.6$ MPa flows through a nozzle, its theoretical exit velocity is about $v_A = 491$ m/s.

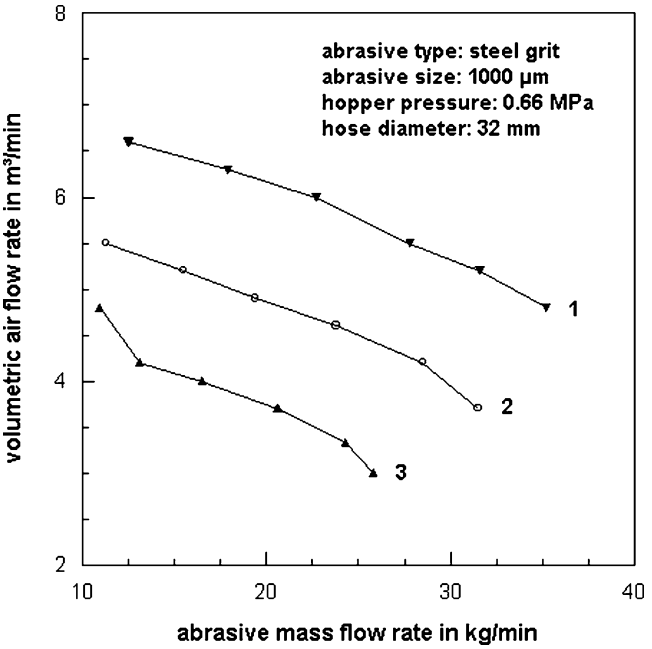

Fig. 3.11 Effects of abrasive mass flow rate and nozzle geometry on the air volume flow rate in convergent–divergent nozzles (Bae et al., 2007). Nozzle "1" – nozzle length: 150 mm, throat (nozzle) diameter: 11.5 mm, divergent angle: 2.1°, convergent angle: 9.3°; Nozzle "2" – nozzle length: 216 mm, throat (nozzle) diameter: 11.0 mm, divergent angle: 1.3°, convergent angle: 7.9°; Nozzle "3" – nozzle length: 125 mm, throat (nozzle) diameter: 12.5 mm, divergent angle: 7.6°, convergent angle: 3.9°

The maximum exit velocity, however, occurs at the point of maximum mass flow rate, which happens under the following conditions: Ψ_{max} and $(p_0/p)_{crit}$ (see Fig. 3.5). If the Laval pressure ratio $(p_0/p)_{crit}$ is introduced into (3.20), the following maximum limit for the air velocity in parallel cylindrical nozzles results:

$$v_{A\,max} = \left(2 \cdot \frac{\kappa}{\kappa + 1} \cdot \frac{p}{\rho_A}\right)^{1/2} \tag{3.21}$$

After further treatment, the final equation reads as follows:

$$v_{A\,max} = v_L = (\kappa \cdot R_i \cdot T)^{1/2} \tag{3.22}$$

The equation is equal to (3.9). This critical air velocity is frequently referred to as *Laval velocity* (v_L). It cannot be exceeded in a cylindrical nozzle. It depends not on pressure, but on gas parameters and gas temperature. Figure 3.4 presents results for calculated Laval velocities. For the example mentioned in relationship with (3.20), the critical air flow velocity is $v_L = 347$ m/s, which is much lower than the velocity of $v_A = 491$ m/s calculated with (3.20).

If the exit air velocity needs to be increased further in order to exceed the Laval velocity given by (3.22), the nozzle exit region must be designed in a divergent shape. Nozzles which operate according to this design were independently developed by the German engineer Ernst Körting (1842–1921) and the Swedish engineer Gustav de Laval (1845–1913). In honour of the latter inventor, they are called Laval nozzles.

3.2.4 Air Flow in Laval Nozzles

If air velocities higher than the Laval velocity ($v_A > v_L$) are to be achieved, the cross-section of the nozzle must be extended in a way that smooth adiabatic expansion of the air is possible. Such a nozzle geometry is called convergent–divergent (Laval) nozzle. An example is shown in Fig. 3.12. The figure shows an image that was taken with X-ray photography. The flow direction is from right to left. The nozzle consists of a convergent section (right), a throat (centre) and a divergent section (left). The diameter of the throat, which has the smallest cross-section in the system, is considered the nozzle diameter (d_N). For this type of nozzle, (3.20) can be applied without a restriction. For practical cases, a nozzle coefficient φ_L should be added, which delivers the following equation for the calculation of the exit velocity of the air flow:

$$v_A = \varphi_L \cdot \left(2 \cdot \frac{\kappa}{\kappa - 1} \cdot \frac{p}{\rho_A} \cdot \left[1 - \left(\frac{p_0}{p} \right)^{\frac{\kappa-1}{\kappa}} \right] \right)^{1/2} \tag{3.23}$$

The Laval nozzle coefficient φ_L is a function of a dimensionless parameter ω. Relationships for two nozzle qualities are exhibited in Fig. 3.13. The parameter ω depends on the pressure ratio p_0/p (Kalide, 1990). Examples for certain pressure levels are plotted in Fig. 3.14. It can be seen that the dimensionless parameter takes values between $\omega = 0.5$ and 1.0 for typical blast cleaning applications. The parameter ω decreases if air pressure increases. A general trend is that nozzle efficiency decreases for higher air pressures. Results of (3.23) are displayed in the left graph in Fig. 3.15. The right graph displays results of (3.22). One result is that air flowing through a cylindrical nozzle at a high temperature of $\vartheta = 200°C$ and at a rather low pressure of $p = 0.2$ MPa obtains an exit velocity which is equal to that of air which

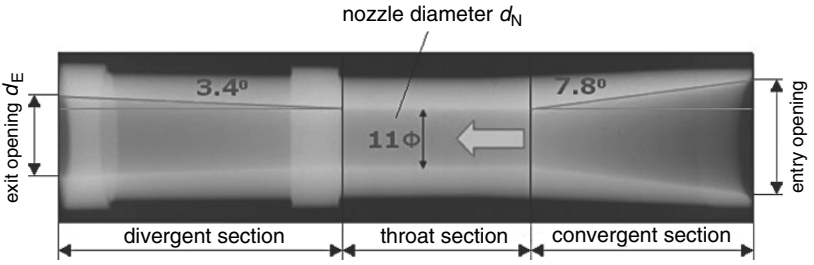

Fig. 3.12 X-ray image of a convergent–divergent (Laval) nozzle design (Bae et al., 2007)

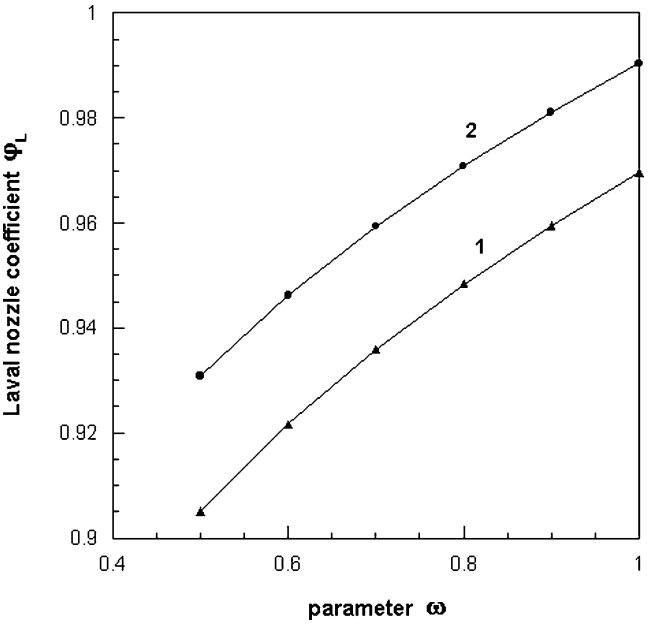

Fig. 3.13 Relationship between φ_L and ω (Kalide, 1990). "1" – Straight nozzle with smooth wall; "2" – curved nozzle with rough wall

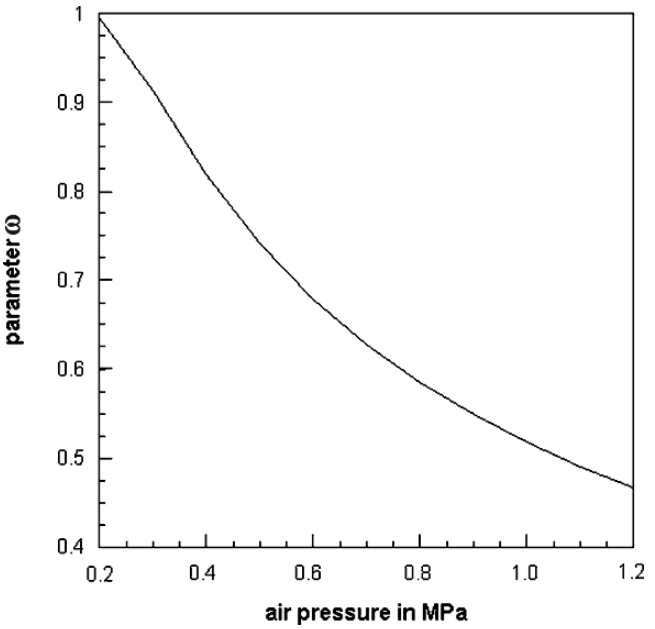

Fig. 3.14 Function $\omega = f(p)$ for $p_0 = 0.1$ MPa; according to a relationship provided by Kalide (1990)

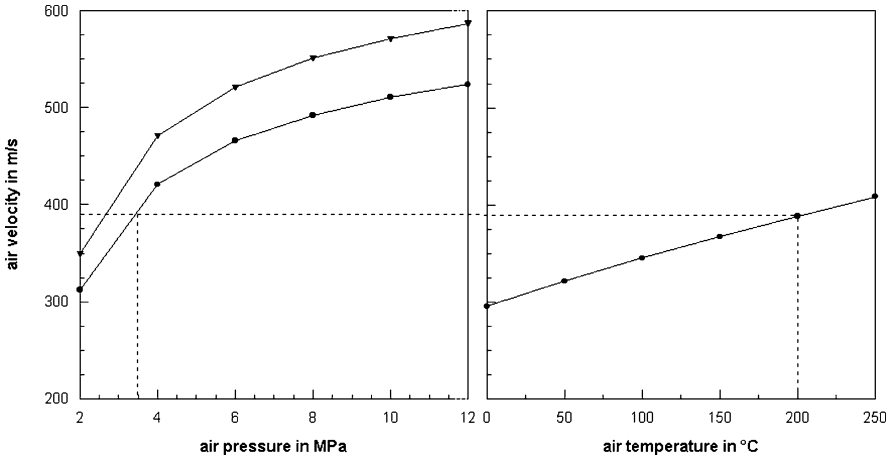

Fig. 3.15 Theoretical air exit velocities in Laval nozzles. Left: air temperature effect; upper curve: ϑ =100°C; lower curve: $\vartheta = 20°C$; Right: air pressure effect; $p = 0.2\,\text{MPa}$

is flowing through a Laval nozzle at a temperature of $\vartheta = 20°C$ and at a much higher pressure of $p = 0.35\,\text{MPa}$.

The air mass flow rate through a Laval nozzle can be calculated with (3.14), whereby d_N is the diameter of the narrowest cross-section (throat) in the nozzle. For air at a pressure of $p = 0.6\,\text{MPa}$ and a temperature of $\vartheta = 27°C$ ($T = 300\,\text{K}$) flowing through a Laval nozzle with $d_N = 11\,\text{mm}$ and $\alpha_N = 0.95$, (3.14) delivers a mass flow rate of about $\dot{m}_A = 0.133\,\text{kg/s}$.

The flow and thermodynamics either in cylindrical nozzles or in Laval nozzles can be completely described with commercially available numerical simulation programs, which an example of is presented in Fig. 3.16a. In that example, the progresses of Mach number, air density, air pressure and air temperature along the nozzle length are completely documented. It can be seen that pressure, density and temperature of the air are all reduced during the flow of the air through the nozzle.

The flow regimes that are set up in a convergent–divergent nozzle are best illustrated by considering the pressure decay in a given nozzle as the ambient (back) pressure is reduced from rather high to very low values. All the operating modes from wholly subsonic to underexpanded supersonic are shown in sequences "1" to "5" in Fig. 3.26, which will be discussed later in Sect. 3.4.3.

3.2.5 Power, Impulse Flow and Temperature

The power of the air stream exiting a nozzle is simply given as follows:

$$P_A = \frac{\dot{m}_A}{2} \cdot v_A^2 \tag{3.24}$$

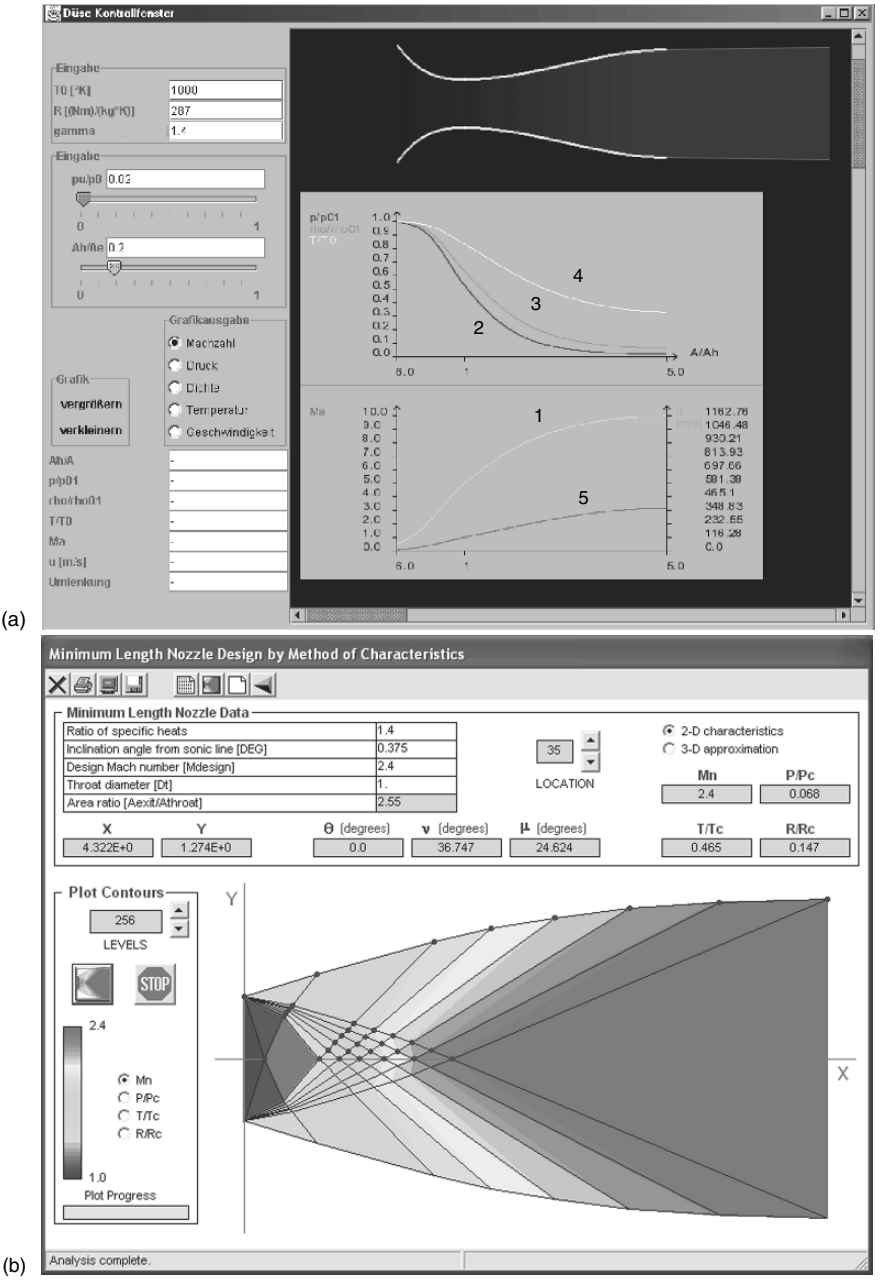

Fig. 3.16 Results of numerical simulations of the air flow in convergent–divergent nozzles (Laval nozzles). (**a**) Gradients for Mach number (1), pressure (2), density (3), temperature (4) and air velocity (5): image: RWTH Aachen, Aachen, (Germany); (**b**) Complete numerical nozzle design including shock front computation (Aerorocket Inc., Citrus Springs, USA)

For the above-mentioned example, the air stream power is about $P_A = 16\,kW$. The impulse flow of an air stream exiting a nozzle can be calculated as follows:

$$\dot{I}_A = \dot{m}_A \cdot v_A \tag{3.25}$$

For the parameter combination mentioned above, the impulse flow is about $\dot{I}_A = 65\,N$.

Because of the air expansion, air temperature drops over the nozzle length (see Fig. 3.16a). The temperature of the air at the nozzle exit can be calculated based on (3.19). A manipulation of this equation delivers the following relationship (Bohl, 1989):

$$T_E = T_N - \frac{v_A^2}{2 \cdot c_P} \tag{3.26}$$

In that equation, T_N is the entry temperature of the air. The value for the isobaric heat capacity of air is listed in Table 3.1. For the above-mentioned example, (3.26) delivers an air exit temperature of $T_E = 180\,K$ ($\theta_E = -93°C$).

3.3 Abrasive Particle Acceleration in Nozzles

3.3.1 General Aspects

Solid abrasives particles hit by an air stream do accelerate because of the drag force imposed by the air stream. The situation is illustrated in Fig. 3.17 where results of a numerical simulation of pressure contours and air streamlines around a sphere are shown. The acceleration of the sphere is governed by Newton's second law of motion:

$$m_P \cdot \frac{dv_P}{dt} = F_D = c_D \cdot A_P \cdot \frac{\rho_A}{2} \cdot |v_A - v_{P0}|^2 \tag{3.27}$$

The drag force F_D depends on the particle drag coefficient, the average cross-sectional area of the particle, the density of the air and on the relative velocity between air and particle. The term $|v_A - v_{P0}| = v_{rel}$ is the relative velocity between gas flow and particle flow. For very low particles flow velocities, for example, in the entry section of a nozzle, $v_{rel} = v_A$. The term $1/2 \cdot \rho_A \cdot v_{rel}^2$ is equal to the dynamic pressure of the air flow.

The drag coefficient is usually unknown and should be measured. It depends on Reynolds number and Mach number of the flow: $c_D = f(Re,\ Ma)$, whereby the Mach number is important if the air flow is compressible. Settles and Geppert (1997) provided some results of measurements performed on particles at supersonic speeds.

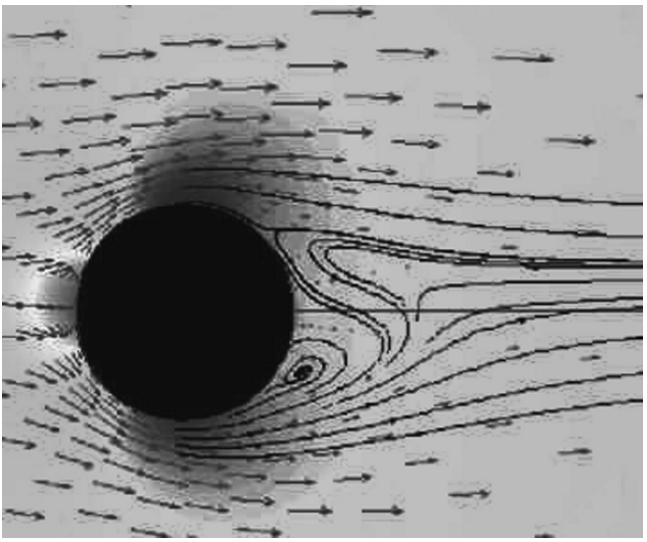

Fig. 3.17 Numerically simulated pressure contours and flow streamlines on a solid particle in a high-speed air flow (image: H.A. Dwyer, University of California, Davis)

Their results, plotted in Fig. 3.18, suggest that the drag coefficient only weakly depends on Reynolds number, but is very sensitive to changes in the Mach number. The c_D-value is rather low at low Mach number values, but it dramatically increases after a value of $Ma = 1$. It finally levels off around a value of unity for Mach numbers greater than $Ma = 1.4$. More information on this issue is delivered by Bailey and Hiatt (1972), who published c_D–Ma–Re data for different nozzle geometries, and by Fokke (1999). Other notable effects on the drag coefficient are basically those

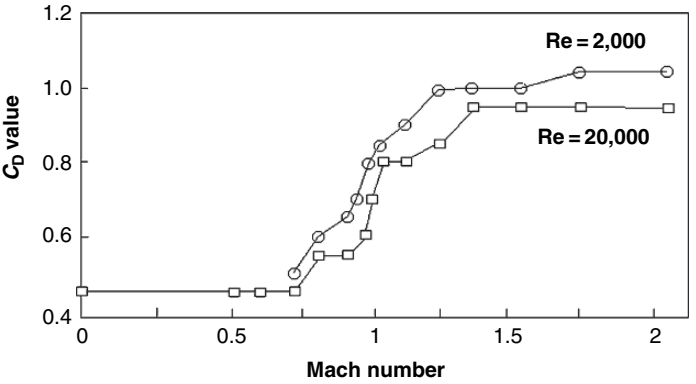

Fig. 3.18 Effects of Mach number and Reynolds number on friction parameter (Settles and Geppert, 1997)

of acceleration, of particle shape and of particle shielding, which are discussed in Brauer's (1971) book.

The air density is, in the first place, a function of pressure and temperature as expressed by (3.6). This is an interesting point because both parameters notably vary over the nozzle length as witnessed by the results of numerical simulations provided in Fig. 3.16a. Both air pressure and air temperature drop if they approach the exit. The relative velocity can, for practical purposes, be replaced by the velocity of the air flow ($v_A \gg v_{P0}$), if the acceleration process starts. In cylindrical nozzles, this velocity cannot exceed the speed of sound (see Sect. 3.2). However, because speed of sound depends on gas temperature (3.9), a theoretical possibility for an increase in drag force due to gas temperature increase exists.

The acceleration acting on a particle during the particle–air interaction can be approximated as follows:

$$a_P = \dot{v}_P = \frac{F_D}{m_P} \tag{3.28}$$

This condition delivers the following relationship:

$$\dot{v}_P \propto \frac{c_D \cdot \rho_A \cdot v_A^2}{d_P \cdot \rho_P} \tag{3.29}$$

Acceleration values for convergent–divergent nozzles were calculated by Achtsnick (2005), who estimated values as high as $a_P = 10^7$ m/s^2. This author could also verify the trend expressed in (3.29) for the particle diameter. The particle acceleration increased extraordinarily when the abrasive particle diameter was reduced below $d_P = 10$ µm. If particles get smaller, they start to follow the trajectories of air flow they are suspended, and the slip between particles and air flow reduces. The acceleration period required to realise a given final particle speed can be approximated as follows:

$$t_a \propto \frac{v_P \cdot d_P \cdot \rho_P}{c_D \cdot \rho_A \cdot v_A^2} \tag{3.30}$$

Acceleration is, of course, not a constant value over the nozzle length, but (3.29) depicts that acceleration effects are, in general, less severe if particles with larger diameter and larger density are entrained into the air flow. For a desired particle speed, acceleration period (nozzle length) must be increased if heavy (ρ_P), respectively large (d_P), abrasive particles are injected. Acceleration period (nozzle length) can be reduced if air flow density (ρ_A), air flow velocity (v_A) and drag coefficient (c_D) feature high values.

Equation (3.27) must be solved by numerical methods, and numerous authors (Kamzolov et al., 1971; Ninham and Hutchings, 1983; Settles and Garg, 1995; Settles and Geppert, 1997; Johnston, 1998; Fokke, 1999; Achtsnick et al., 2005) utilised such methods and delivered appropriate solutions. Results of such calculation procedures are provided in the following sections.

3.3.2 Simplified Solution

Iida (1996) and Kirk (2007) provided an approximation for the velocity of particles accelerated in a cylindrical blast cleaning nozzle. The solution of Iida (1996) neglects effects of friction parameter and air density. Kirk's (2007) approximation reads as follows:

$$\left(\frac{v_P}{v_A - v_P}\right)^2 = \frac{c_D \cdot L_N}{d_P} \cdot \frac{\rho_A}{\rho_P} \tag{3.31}$$

Due to certain simplifications, this equation can only serve for the assessment of trends, but cannot deliver suitable quantitative results. A solution to (3.31) delivers the following trends:

$$v_P \propto p^{0.68} \tag{3.32a}$$

$$v_P \propto d_P^{-0.36} \tag{3.32b}$$

$$v_P \propto \rho_P^{-0.38} \tag{3.32c}$$

Uferer (1992) applied a simplified numerical procedure for the calculation of abrasive particles accelerated in blast cleaning nozzles. Some results of these calculations for two nozzle layouts are provided in Fig. 3.19. The graphs demonstrate that the utilisation of a Laval nozzle increases the velocities of air and abrasive particles, but the gain is much higher for the air acceleration. The reason is the drop in air density in the divergent section of the Laval nozzle (see Fig. 3.16a). According to (3.27), this causes a reduction in the drag force acting at the particles to be accelerated. Thus, although Laval nozzles are very efficient in air acceleration, they do not increase the abrasive exit speed at an equally high ratio.

3.3.3 Abrasive Flux Rate

The abrasive flux rate through a nozzle (in kg/s per unit nozzle area passing through the nozzle) can be approximated as follows (Ciampini et al., 2003b):

$$\dot{m}_N = \rho_P \cdot v_P \cdot \rho_S^* \tag{3.33}$$

Thus, for a given abrasive material and incident abrasive velocity, interference effects resulting from changes in flux are described by the dimensionless stream density (see Sect. 3.5.5).

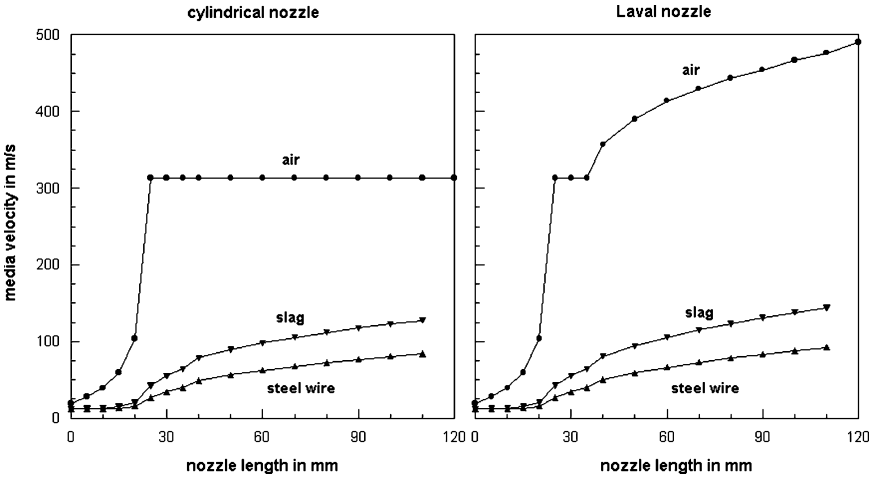

Fig. 3.19 Effects of nozzle layout on calculated air and abrasive velocities (Uferer, 1993)

3.3.4 Abrasive Particle Spacing

The average distance between individual abrasive particles in a blast cleaning nozzle can be approximated as follows (Shipway and Hutchings, 1994):

$$L_P = \left(\frac{m_P \cdot v_P \cdot \pi \cdot r_N^2}{\dot{m}_P} \right)^{1/3} \tag{3.34}$$

Results obtained by Shipway and Hutchings (1994) are listed in Table 3.5. The ratio between spacing distance and abrasive particle diameter had a typical value of about $L_P/d_P = 15$. For a low abrasive mass flow rate, this value increased up to $L_P/d_P = 23$.

Table 3.5 Average distances between abrasive particles in a blast cleaning nozzle (Shipway and Hutchings, 1994)

Particle diameter in µm	Particle velocity in m/s	Abrasive mass flow rate in g/min	Average distance in µm	L_P/d_P
63–75	70	50	900	~ 13
125–150	52	6	3,200	~ 23
212–250	45	31	4,000	~ 17
650–750	29	37	7,900	~ 13

3.4 Jet Structure

3.4.1 Structure of High-speed Air Jets

A schematic sketch of a free air jet is shown in Fig. 3.20. The term "free jet" designates systems where a fluid issues from a nozzle into a stagnant medium, which consists of the same medium as the jet. Two main regions can be distinguished in the jet: an initial region and a main region. The *initial region* is characterised by a potential core, which has an almost uniform mean velocity equal to the exit velocity. The velocity profile is smooth in that region. Due to the velocity difference between the jet and the ambient air, a thin shear layer forms. This layer is unstable and is subjected to flow instabilities that eventually lead to the formation of vertical structures. Because of the spreading of the shear layer, the potential core disappears at a certain stand-off distance. Ambient air entrains the jet, and entrainment and mixing processes continue beyond the end of the potential core. In the *main region*, the radial velocity distribution in the jet finally changes to a pronounced bell-shaped velocity profile as illustrated in Fig. 3.20. The angle θ_J is the expansion angle of the jet. In order to calculate this angle, the border between air jet and surrounding air flow must be defined. One definition is the half-width of the jet defined as the distance between the jet axis and the location where the local velocity $[v_J(x,r)]$ is equal to the half of the local maximum velocity situated on the centreline $[v_J(x, r = 0)]$. Achtsnick (2005) who applied this definition estimated typical expansion angles between $\theta_J = 12.5^\circ$ and 15°.

Shipway and Hutchings (1993a) took schlieren images from acetone-air plumes exiting cylindrical steel nozzles at rather low air pressures up to $p = 0.09$ MPa, and they could prove that the plume shape differed just insignificantly if the gas exited either from a nozzle with a low internal roughness ($R_a = 0.25$ µm) or from a nozzle with a rough wall structure ($R_a = 0.94$ µm). This situation changed if abrasive particles were added to the air flow.

The structure of an abrasive jet is disturbed due to rebounding abrasive particles if the nozzle is being brought very close to the specimen surface. This was

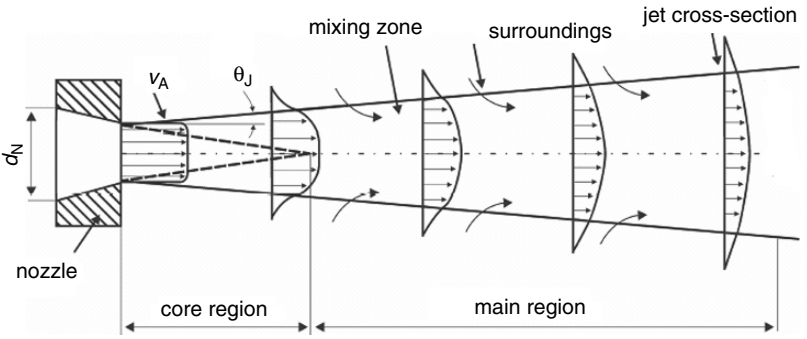

Fig. 3.20 Structure of an air jet issued from a nozzle into stagnant air (adapted from Achtsnick, 2005)

verified by Shipway and Hutchings (1994) who took long-exposure photographs of the trajectories of glass spheres in an air jet and observed many particle trajectories, which deviated strongly from the nozzle axis. It was supposed that these are particles rebounding from the target.

3.4.2 Structure of Air-particle Jets

Plaster (1972) was probably the first who advised the blast cleaning industry into the effect of nozzle configuration on the structure of air-particle jets. The images shown in Fig. 3.21 clearly illustrate the influence of nozzle design on jet stability. Figure 3.21a shows a jet exiting from a badly designed nozzle, which results in a shock wave at the tip (central image) and in an erratic projection of abrasives (right image). A correctly designed nozzle is shown in Fig. 3.21b. This nozzle produces a smooth flow as can be seen by the configuration of the air stream (central image) and by the even projection of the abrasives (right image).

The width (radius) of high-speed air-particle jets at different jet lengths was measured by Fokke (1999) and Slikkerveer (1999). Kirk and Abyaneh (1994) and Slikkerveer (1999) provided an empirical relationship as follows:

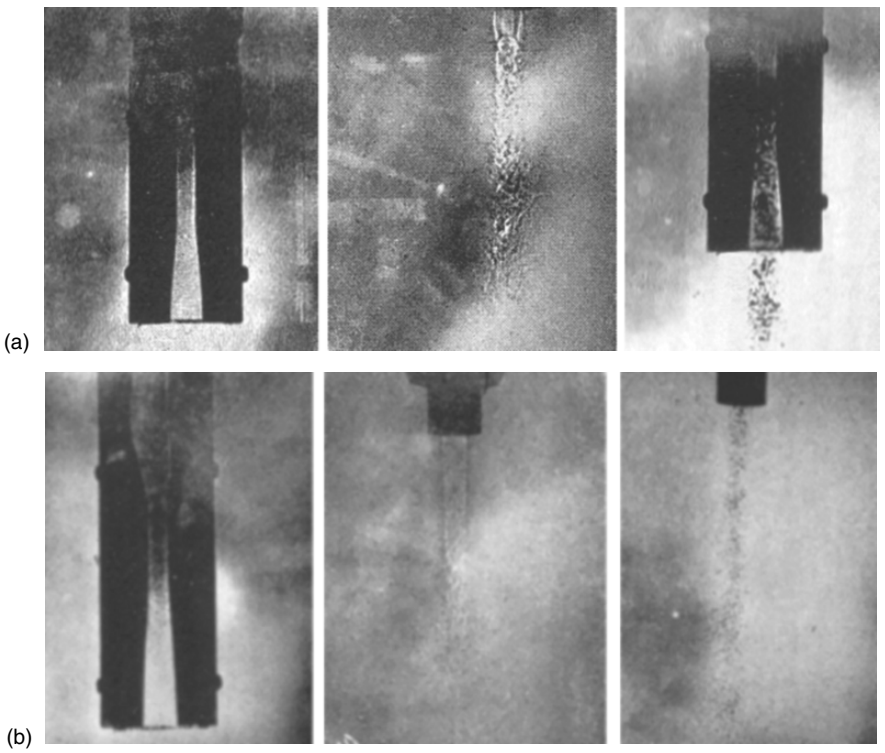

Fig. 3.21 Effect of nozzle design on jet structure and abrasive acceleration (Plaster, 1972). (**a**) Badly designed nozzle; (**b**) Correctly designed nozzle

$$d_J = d_N + 2 \cdot x \cdot \tan \theta_J \tag{3.35}$$

The expansion angle can be considered to be between $\theta_J = 3^\circ$ and 7° (Slikkerveer, 1999; Achtsnick et al., 2005). Therefore, it is smaller than for a plain air jet. Results of calculations based on (3.35) for $\theta_J = 5^\circ$ are displayed in Fig. 3.22.

Fokke (1999) found an almost linear relationship between jet half width and jet length. The air mass flow rate showed marginal effects on the half width at longer jet lengths: with an increase in air mass flow rate, half width slightly decreased. Some relationships are illustrated in Fig. 3.23. These results corresponded to that of Mellali et al. (1994) who found a linear relationship between stand-off distance and the area of the cross-section hit by a blast cleaning jet.

Shipway and Hutchings (1993a) took schlieren images from glass bead plumes exiting cylindrical steel nozzles at air pressures up to $p = 0.09$ MPa. They noted a distinct effect of the nozzle wall roughness on the plume shape as a result of the differences in the interaction of the particles with the nozzle wall. Variations in the rebound behaviour of the glass beads on impact with the nozzle wall caused the particles to leave the nozzle exit with different angular distributions. These authors also defined a "plume spread parameter", respectively a "focus coefficient":

$$\beta_P = \alpha_P \cdot x \tag{3.36}$$

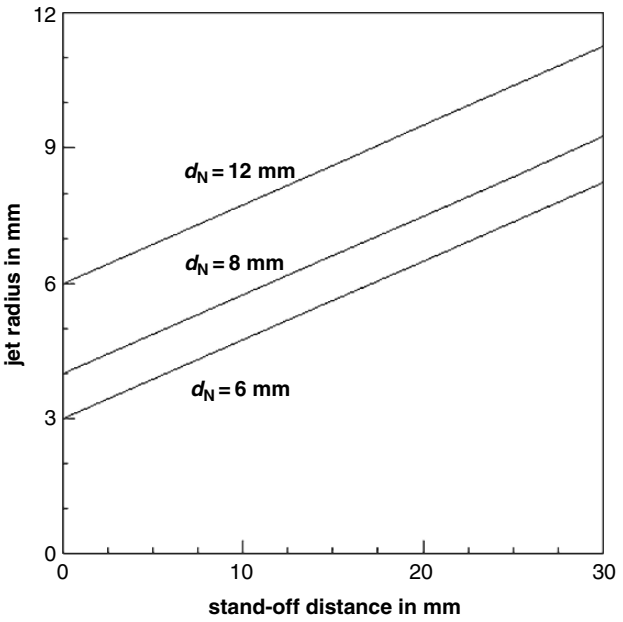

Fig. 3.22 Radius of a particle-air jet according to (3.35)

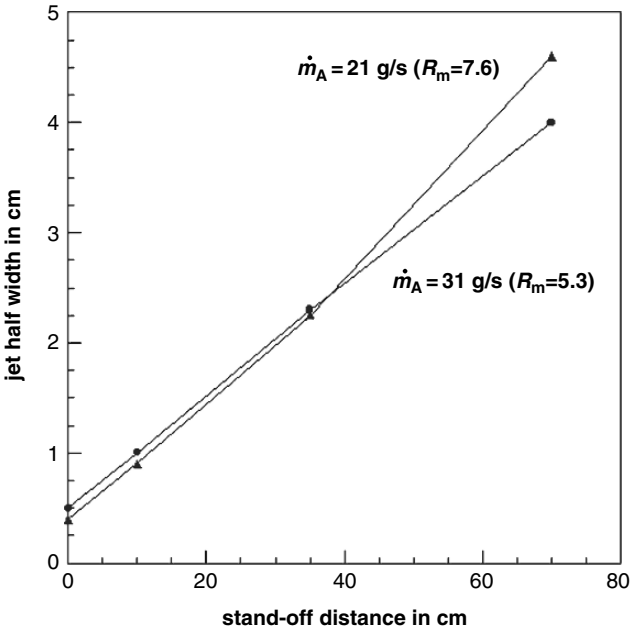

Fig. 3.23 Effects of stand-off distance and air mass flow rate (respectively mass flow ratio abrasive/air) on jet radius (Fokke, 1999)

Here, α_P is a constant that depends on the nozzle configuration. Lower values for α_P mean less spread and vice versa. Shipway and Hutchings (1993a) provided a method for the estimation of the dimensionless *focus coefficient*. It could be shown experimentally that the focus coefficient depended on the roughness of the nozzle wall surface. Results of this investigation are listed in Table 3.6. It was also shown by Stevenson and Hutchings (1995b) that the focus coefficient depended on nozzle length and abrasive particle velocity. It exhibited maximum values at moderate nozzle lengths. If abrasive particle velocity increased, the focus coefficient decreased notably.

3.4.3 Design Nozzle Pressure

Each Laval nozzle (convergent–divergent nozzle) has a so-called *design nozzle pressure* that enables it to produce a supersonic jet of air into the atmosphere with

Table 3.6 Relationships between nozzle wall roughness, abrasive particle type and *focus coefficient* (Shipway and Hutchings, 1993a)

Wall roughness in μm	Focus coefficient	
	Silica	Glass beads
0.94	14	8.7
0.25	22.3	15.2

minimum disturbance. The design criterion is the air pressure at the nozzle exit (P_E). The value for this pressure should be equal to the pressure of the surrounding air (called *back pressure* in the flow dynamics literature). The situation is characterised by the curve "1" in Fig. 3.26. For blast cleaning applications, the back pressure is usually the atmospheric pressure. The design criterion can be written as follows [modified from Bohl's (1989) book]:

$$\left(\frac{d_E}{d_N}\right)^2 = \left(\frac{\kappa+1}{2}\right)^{\frac{1}{\kappa-1}} \cdot \left(\frac{p_E}{p}\right)^{\frac{1}{\kappa}} \cdot \left\{\frac{\kappa+1}{\kappa-1} \cdot \left[1-\left(\frac{p_E}{p}\right)^{\frac{\kappa-1}{\kappa}}\right]\right\}^{1/2} \tag{3.37}$$

For $p_E = p_0$, this equation delivers a ratio between exit diameter and nozzle (throat) diameter, which must be maintained in order to allow an undisturbed air flow at the given nozzle inlet pressure. A graphical solution to (3.37) is provided in Fig. 3.24. If the nozzle dimensions (d_N, d_E) are known, the corresponding *design pressure* can be read from this graph. Only data points located at the solid line correspond to the expansion condition characterised by Fig. 3.25d and by line "1" in Fig. 3.26.

It must be noted, however, that these relationships apply to the flow of plain air only. If solid particles are added, the effects of the particle flow must be considered. Fokke (1999) performed numerical simulations of the nozzle flow, and he could show that the addition of abrasive particles (steel balls, d_P = 50–1,000 µm;

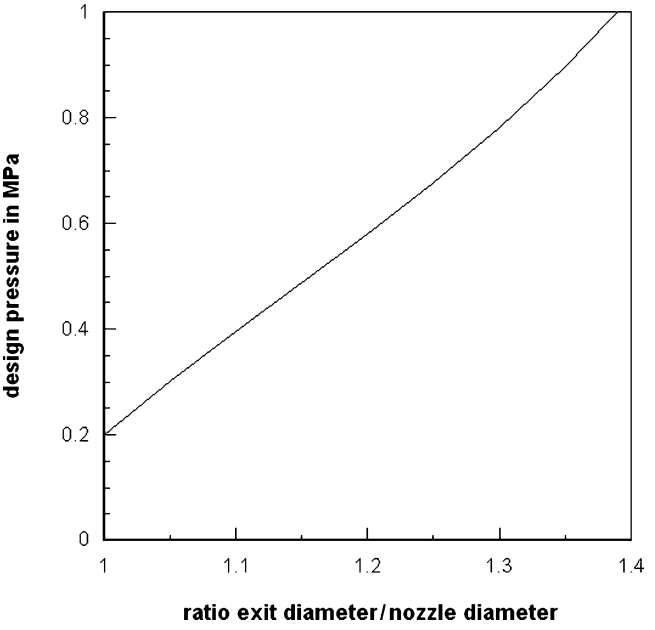

Fig. 3.24 Relationship between nozzle geometry and design pressure for convergent–divergent nozzles. Based on (3.37)

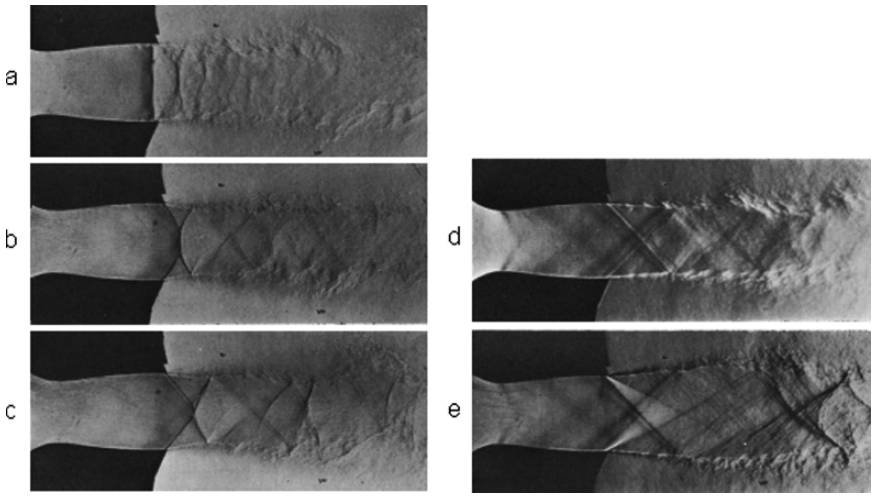

Fig. 3.25 Flow situation near the exit of a convergent–divergent nozzle (Oosthuizen and Carscallen, 1997) (**a**) Overexpanded flow with shock front leaving the nozzle exit; (**b**) Overexpanded flow with disappearing normal central shock front outside the nozzle; (**c**) Overexpanded with oblique shocks outside the nozzle; (**d**) Almost isentropic nozzle flow; (**e**) Underexpanded flow with severe expansion waves outside the nozzle

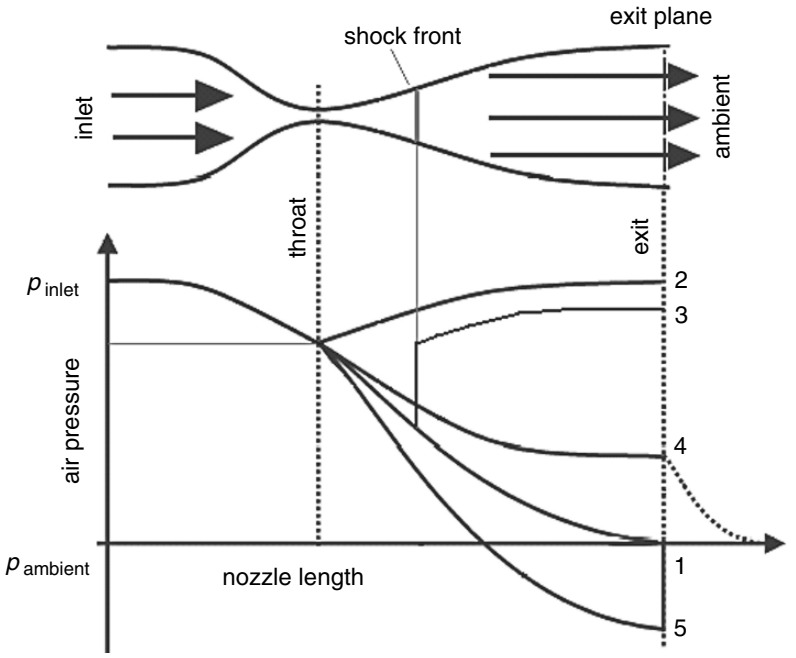

Fig. 3.26 Operating conditions of a convergent–divergent nozzle; see text for "1" to "5" (adapted from Oertel, 2001)

R_m = 0.1–6) was sensitive to the nozzle exit pressure. For all loading ratios, exit pressure increased with decreasing particle size. Exit pressure also increased with an increase in the mass flow ratio abrasive/air. Although the nozzle in Fokke's (1999) work was designed in a way that the air exit pressure would meet the atmospheric pressure, the exit pressures were all well below the atmospheric pressure as the abrasive particles were added. Effects of abrasive particle on the gas flow properties in the nozzle vanished for small mass flow rates abrasive/air ($R_m \ll 1$).

It is recommended to run a Laval nozzle at least at the design pressure for the nozzle being used, and at higher pressure if possible. When the nozzle is operated below the design pressure, the flow forms shock waves that slow down air flow as well as abrasive particles. Schlieren optics has been utilised by several authors to reveal such shock wave structures (Settles and Garg, 1995; Mohamed et al., 2003; Kendall et al., 2004). Some images are provided in Figs. 3.25 and 3.27.

Figure 3.26 summarises possible pressure decay modes along a convergent–divergent nozzle operating between nozzle inlet pressure and ambient pressure. Up to the throat, in the divergent section, the nozzle pressure decreases for all flow conditions. If the nozzle is being designed in a way that the nozzle exit pressure meets the atmospheric (back) pressure, the gas exits the nozzle as an undisturbed flow with parallel flow patterns. The flow is isentropic and shock-free. This situation is illustrated through the curve "1" in Fig. 3.26 and the image in Fig. 3.25d. In the situation characterised by the line "2" in Fig. 3.26, the back pressure is higher than the nozzle exit pressure (and also higher than the Laval pressure), but is reduced sufficiently to make the flow reach sonic conditions at the throat ($Ma = 1$). The flow in the divergent section is still subsonic because the back pressure is still high. Under ideal flow conditions (no friction), the exit nozzle pressure is equal to the

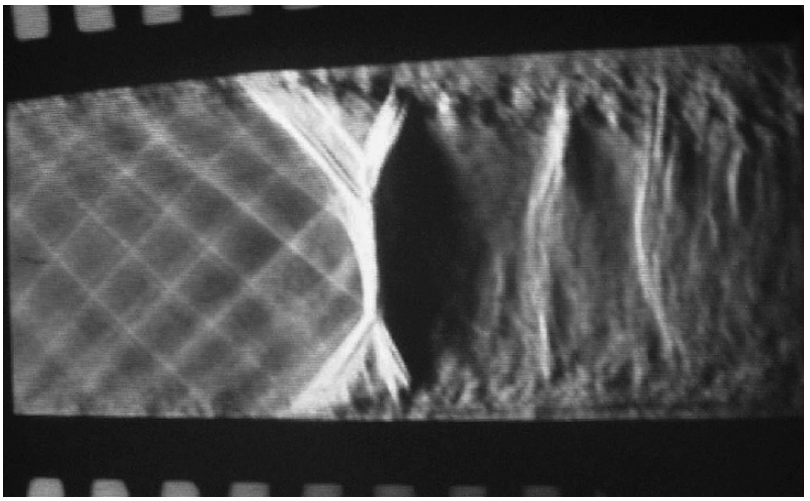

Fig. 3.27 Shock wave in the divergent section of a nozzle, followed by flow separation (image: Mechanical and Aerospace Engineering, University of California, Irvine)

nozzle entry pressure. The line "3" illustrates the situation if the back pressure is further reduced. In that case, a compression shock occurs in the flow in the divergent section of the nozzle. An example for such a shock front is provided in Fig. 3.27. This compression shock front in the divergent part of the nozzle develops normal to the flow, and it generates a "pressure jump", which is illustrated by the vertical line between line "1" and line "3" in Fig. 3.26. In front of this shock front, the flow is supersonic, whereas the flow behind the shock front moves at subsonic speed. Precise location and strength of the shock front depend on the back pressure. Decreasing the back pressure moves the shock wave downstream, and it finally reaches the nozzle exit plane (see image in Fig. 3.25a). If the back pressure is further reduced, the shock wave moves outside the nozzle, and the "pressure jump" takes places through a series of oblique shock waves. This type of nozzle flow is termed *over-expanded*. Line "4" in Fig. 3.26 and the images in Fig. 3.25b and c illustrate this case. The central shock wave head is at an almost normal position as shown in Fig. 3.25b, but the shock trajectories start to incline as in Fig. 3.25c for the lower back pressure. If the back pressure is further reduced and becomes less than the nozzle exit pressure, the flow expands, and the expansion takes place through a series of expansion waves outside the nozzle. This case is expressed through the line "5" in Fig. 3.26. Such a nozzle flow is termed *under-expanded*. Figure 3.25e provides an example. The system of expansion waves can clearly be distinguished in front of the nozzle exit. More illustrative photographs for the different types of pressure distribution can be found in Oertel (2001), where some very early schlieren images, taken by Ludwig Prandtl in 1907, are presented.

It was found, however, by some investigators that air expansion regime and shock location depended on abrasive parameters as well, namely on abrasive mass flow rate and abrasive particle size and density (Komov 1966; Myshanov and Shirokov, 1981; Fokke, 1999; Achtsnick et al., 2005). Komov (1966) found that the degree of air expansion was less for a particle-laden flow compared with the plain gas flow. This difference increased as the mass flow ratio abrasive/air increased. The authors also took images from shock fronts in a flow of air as well as in a particle-laden air flow, and they found that the shock front in the particle-laden air flow was located further upstream. They noted that this effect was most pronounced for high mass flow rates abrasive/air and smaller particles.

The operating characteristics of convergent nozzles and convergent–divergent nozzles are in detail described and discussed by Oosthuizen and Carscallen (1997). Schlieren images of shock waves formed in nozzles and in the exiting air jets under certain operating conditions can be found in Oertel's (2001) book. Examples of air jets formed under different operating conditions are shown in Fig. 3.25. Sakamura et al. (2005) have shown that pressure-sensitive paint technique can very well capture pressure maps for the two-dimensional flow in a convergent–divergent nozzle, and these results offer the opportunity for adding more knowledge to this issue. The shock characteristics in blast cleaning nozzles can be modelled with commercially available software programmes. An example is provided in Fig. 3.16b.

3.5 Composition of Particle Jets

3.5.1 Radial Abrasive Particle Distribution

Adlassing (1960) designed a special device for the assessment of the radial distribution of abrasive particles in an air jet exiting from blast cleaning nozzles. Interestingly, no distinguished effects of nozzle geometry (e.g. nozzle length) could be noted. General results were as follows: the inner core (24 cm^2 cross-section) consumed between 20 and 25 wt.% of all particles; the medium section (76 cm^2 cross-section) consumed between 45 and 45 wt.% of all abrasives; the external section (2,150 cm^2 cross-section) consumed between 25 and 30 wt.% of all abrasives. A curvature of the entry section of the nozzle did not change the distribution. The width of the particle-occupied section of a jet decreased if air pressure rose.

Particle density distribution over the nozzle exit cross-section is difficult to measure directly, and no systematic experimental study is known dealing with this issue. Achtsnick (2005) has subjected a polished glass plate to an abrasive particle flow formed in a blast cleaning nozzle. The visible impacts were microscopically detected and counted regardless their sizes. The results are presented in Fig. 3.28, and they demonstrated that the particles were essentially centred near the nozzle axis. Outside the centre, the number of impacts decreased sensitively towards the borders of the flow. The resulting particle concentration inside a cylindrical nozzle exit was of a bell-shape type. Outside the circle, drawn in Fig. 3.28, particle impacts occurred only incidentally. The same test was repeated for the perpendicular scanning direction and delivered equal results.

In order to get further information on the particle distribution, numerical simulations have been performed for different nozzle configurations by Achtsnick et al. (2005) and McPhee (2001). Results of these simulations are provided in Figs. 3.29 and 3.30. It can be seen that abrasive particle density distribution notably depended on nozzle layout and abrasive particle size. Effects of nozzle layout are illustrated in Fig. 3.29. According to these images, a Laval nozzle with a modified abrasive entry channel and a rectangular nozzle exit cross-section provided a more even distribution of the particles over the cross-section, whereas the conventional cylindrical nozzle design resulted in a concentration of abrasive particles in the central area of the nozzle cross-section. Some comparative measurements verified these trends (Achtsnick et al., 2005). The images in Fig. 3.30 characterise the effects of abrasive diameter on the particle density distribution in conventional round nozzles. In both cases, particles were concentrated in the centre of the nozzle cross-section, but the particle distribution was more favourable for the smaller abrasives.

3.5.2 Particle Velocity Distribution Function

Achtsnick (2005), Hamed and Mohamed (2001), Linnemann (1997), Linnemann et al. (1996), Slikkerveer (1999), Stevenson and Hutchings (1995) and Zinn et al.

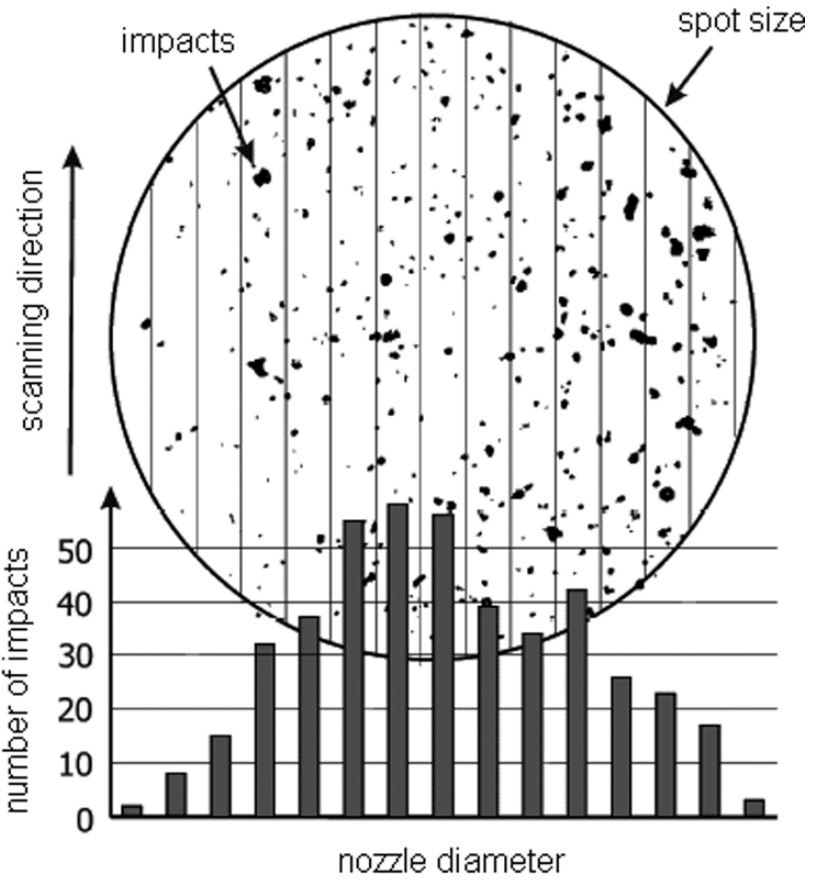

Fig. 3.28 Suggested abrasive particle distribution in the exit plane of a blast cleaning nozzle, based on impact spot inspections (Achtsnick, 2005)

(2002) experimentally investigated the statistical distribution of abrasive particle velocities in air-abrasive jets. The authors found velocity distributions as shown in Figs. 3.31 and 3.32. Figure 3.31 displays results of measurements of the velocities of aluminium oxide powder particles (mesh 360) accelerated in a convergent–divergent nozzle at two different air pressures. As expected, the average particle velocity increased with an increase in air pressure. Similar is the situation for the two graphs plotted in Fig. 3.32. In that case, silica sand particles were accelerated in a convergent-parallel nozzle. A Gaussian normal distribution could be applied to mathematically characterise the distribution of the axial particle velocity:

$$f(v_P) = \frac{1}{\sqrt{2 \cdot \pi} \cdot \sigma_{V_P}} \cdot \exp\left[\frac{-(v_P - \bar{v}_P)^2}{2 \cdot \sigma_{V_P}^2}\right] \tag{3.38}$$

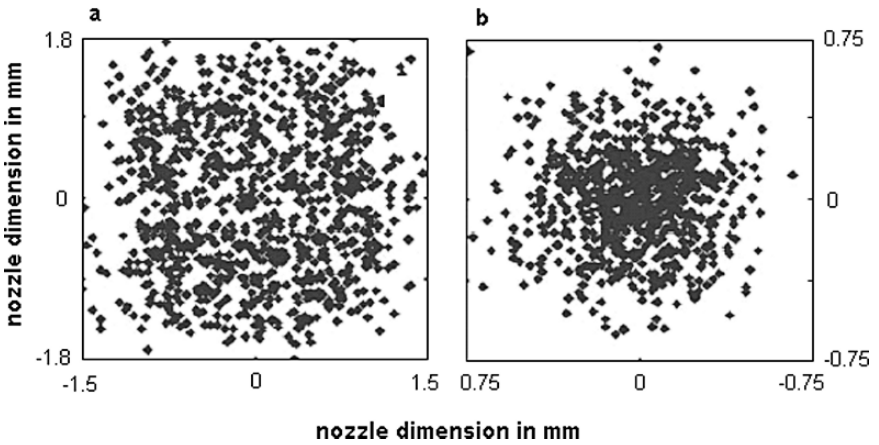

Fig. 3.29 Abrasive particle distributions in the exit planes of blast cleaning nozzles (Achtsnick et al., 2005). (**a**) Square convergent–divergent nozzle; (**b**) Conventional cylindrical nozzle

Typical values were $\bar{v}_P = 75$ m/s for the average axial particle velocity and $\sigma_{VP} = \pm 10$ m/s for the standard deviation of the axial abrasive particle velocity (Stevenson and Hutchings, 1995); and $\bar{v}_P = 15$ m/s for the average axial particle velocity and $\sigma_{VP} = \pm 5$ m/s for the standard deviation of the axial abrasive particle velocity (Linnemann, 1997). Lecoffre et al. (1993) found that the spreading of axial velocity distribution decreased as the nozzle diameter increased. Fokke (1999) has shown that particle velocity standard deviation slightly increased if air pressure rose, and he also found that the standard deviation did not change notably when the mass flow ratio abrasive/air ($R_m = 1.0$–4.5) or the stand-off distance (up to $x = 80$ mm) was varied.

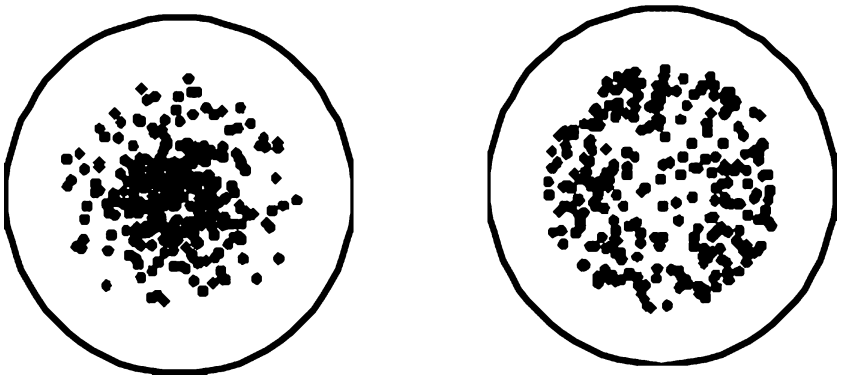

Fig. 3.30 Abrasive particle distributions in the exit plane of a round blast cleaning nozzle (McPhee, 2001). Abrasive material: steel grit; left: $d_P = 820$ µm; right: $d_P = 300$ µm

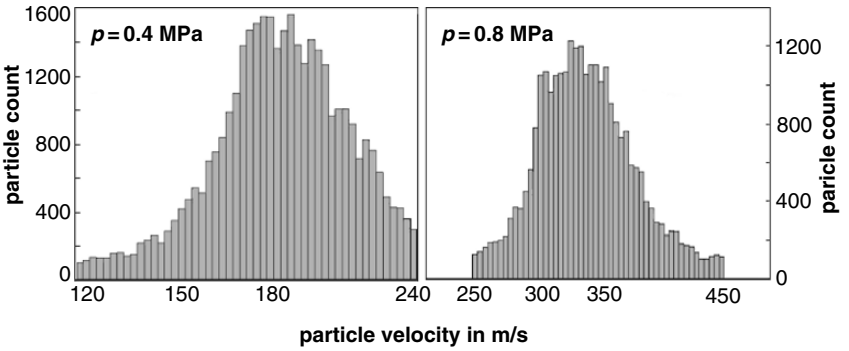

Fig. 3.31 Abrasive particle distributions in abrasive air jets; measurements with aluminium oxide powder (mesh 360) for two pressure levels in a convergent–divergent nozzle (Achtsnick, 2005)

Average particle velocity and abrasive particle velocity standard deviation are not independent on each other; this was shown by Zinn et al. (2002) based on experimental results with rounded-off wire shot. Typical values for the standard deviation were between $\sigma_{VP} = 1.2$ and 2.7 m/s for average abrasive velocities between $\bar{v}_P = 20$ and 47 m/s. The relationships were complex, and parameters which affected these relationships included nozzle type, abrasive particle size and abrasive mass flow rate.

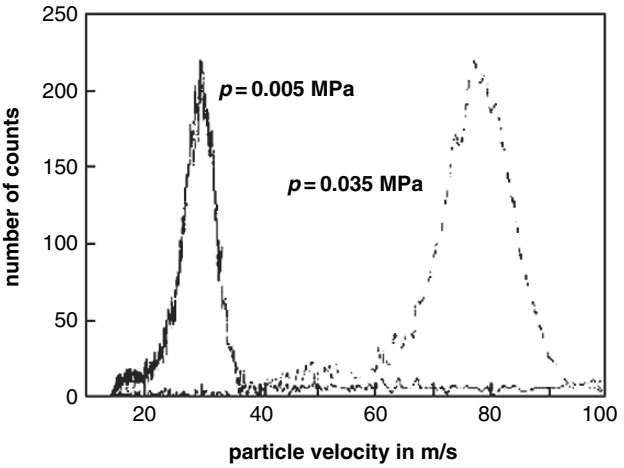

Fig. 3.32 Abrasive particle distributions in abrasive air jets; measurements with silica particles ($d_P = 125$–150 µm) for two low pressure levels in a cylindrical nozzle (Stevenson and Hutchings, 1995). Pressure is gauge pressure

3.5.3 Radial Abrasive Particle Velocity Distribution

Results of measurements of abrasive particle velocities over the cross-sections of two nozzles are plotted in Fig. 3.33. Radial abrasive velocity depended notably on nozzle design and air pressure. It can be seen that the cylindrical nozzle (left graph) featured a typical bell-shaped velocity profile. Such profiles are typical for standard Laval nozzles as well (Johnston, 1998). The modified Laval nozzle with a rectangular cross-section (right graph), however, approached a more favourable rectangular velocity distribution. It can also be seen that high air pressure deteriorated the particle velocity profile. The bell-shape was most pronounced for the highest air pressure.

Figure 3.34 shows results of erosion spot topography measurements performed by Johnston (1998). The term "erosion potential" is equal to the local material

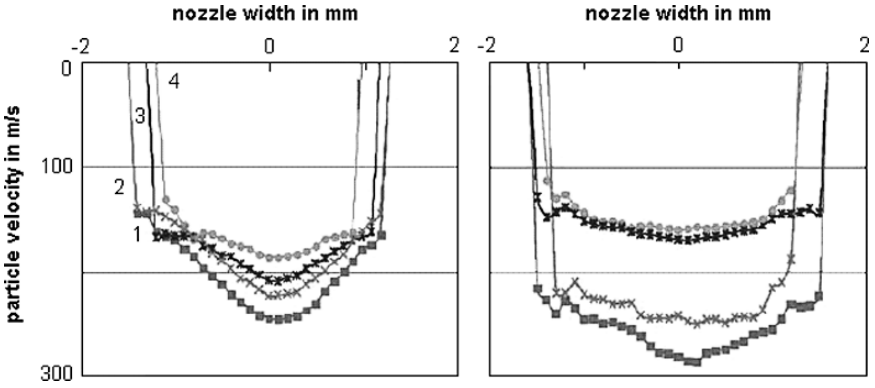

Fig. 3.33 Radial abrasive particle velocity distributions in blast cleaning nozzles (Achtsnick et al., 2005). Left: conventional nozzle; right: square Laval nozzle; Pressure levels: "1" – $p = 0.8$ MPa; "2" – $p = 0.6$ MPa; "3" – $p = 0.5$ MPa; "4" – $p = 0.4$ MPa

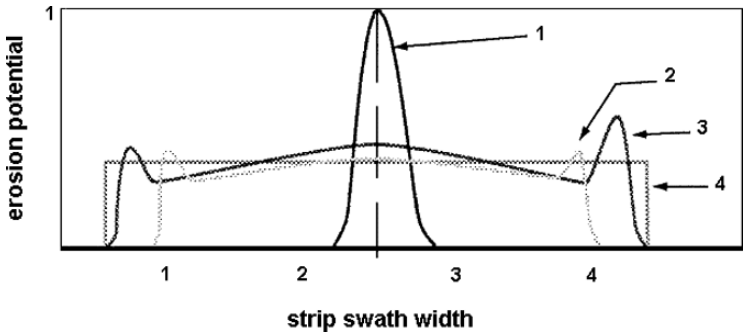

Fig. 3.34 Erosion potential for different nozzle geometries (Johnston, 1998); $p = 0.28$ MPa, $\dot{m}_P = 5.4$ kg/min, $\varphi = 45^\circ$, $x = 51$ mm; "1" – Laval design; "2" and "3": modified nozzles; "4" – ideal distribution

removal depth in a special model material. The standard Laval nozzle (designated "1") generated a small but deep spot formed due to a highly uneven localised erosion potential. The erosion potential was very high at the centre, but was restricted to this central range only. The two "modified" nozzles generated a much more even distribution. The erosion potential was equally distributed over almost the entire width. Only at the rim, there was an increase in the erosion potential. The curve "4" illustrates the erosion potential of an "ideal" blast cleaning nozzle. Here, the erosion potential was equally distributed over the entire strip swath width.

3.5.4 Area Coverage

Aspects of area coverage are illustrated in Figs. 3.35 and 3.36. Figure 3.35 shows images of two dent distributions, whereby the dents are the impressions formed on the target surface due to abrasive particle impingement. Measurements performed by Tosha and Iida (2001) have shown that dent distribution density [dent number/($s \cdot m^2$)] decreased if abrasive particle diameter increased. Figure 3.36 is a typical area coverage graph, where the area coverage is plotted against the exposure time. The area coverage can be calculated as follows (Kirk and Abyaneh, 1994; Karuppanam et al., 2002):

$$C_A(t_E) = 100 \cdot \left[1 - \exp\left(-\frac{3 \cdot r_I^2 \cdot \dot{m}_P \cdot t_E}{4 \cdot A_G \cdot r_P^3 \cdot \rho_P}\right)\right] \tag{3.39}$$

The trend between area coverage and abrasive mass flow rate was experimentally verified by Hornauer (1982). The author also found that values for the area coverage decreased if the traverse rate of the blast cleaning nozzle increased. Because of $t_E \propto v_T^{-1}$, this result also supports the validity of (3.39).

A typical area coverage function can be subdivided into two sections: (1) initial area coverage and (2) full area coverage. This is illustrated in Fig. 3.36. It was experimentally verified (Tosha and Iida, 2001) that the initial area coverage depended, among others, on abrasive particle diameter (initial area coverage dropped if abrasive diameter increased) and abrasive particle velocity (initial area coverage increased if abrasive particle velocity increased). The critical exposure time, where full area coverage started, depended on process parameters as follows (Tosha and Iida, 2001):

$$t_F \propto \frac{d_P^{1/2} \cdot H_M^{1/2}}{v_P} \tag{3.40}$$

3.5.5 Stream Density

Ciampini et al. (2003a) introduced a dimensionless stream density, the geometric basis of which is illustrated in Fig. 3.37a, and derived the following expression:

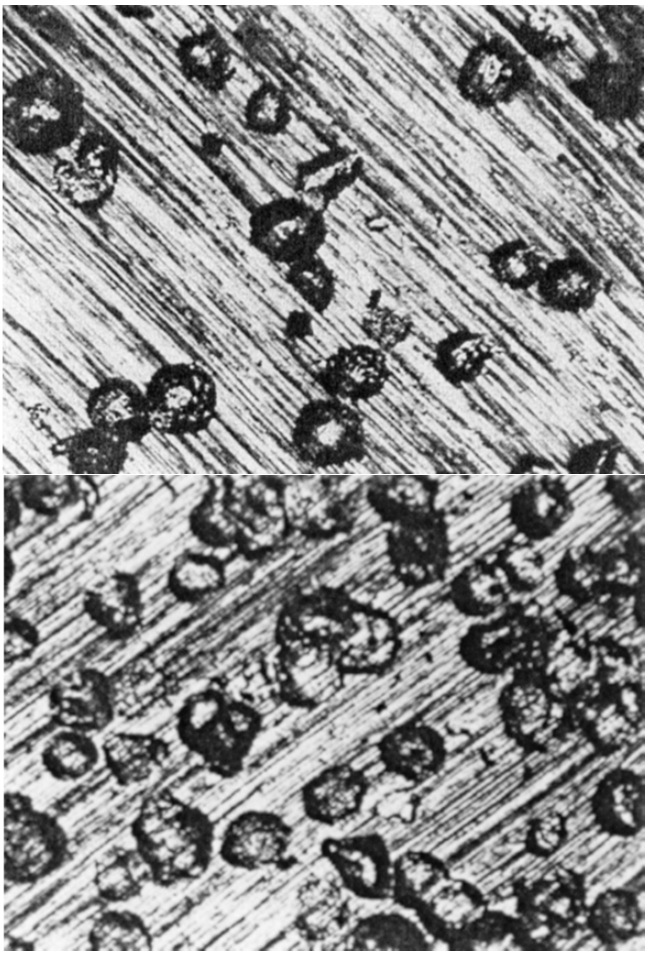

Fig. 3.35 Aspects of area coverage (Meguid and Rabie, 1986). **(a)** Coverage: 16%; **(b)** Coverage: 52%

$$\rho_S^* = \frac{4 \cdot r_P^{*3}}{3 \cdot r_N^{*2} + 3 \cdot r_N^* \cdot x^* \cdot \tan\ \theta_J + x^{*2} \cdot \tan^2 \theta_J} \tag{3.41}$$

The dimensionless numbers in (3.41) read as follows. The dimensionless nozzle radius is defined as follows:

$$r_N^* = \frac{\dot{N}_P \cdot r_N}{v_P} \tag{3.42}$$

It is the number of particles launched in the time taken for a particle of average velocity to travel a distance equal to the nozzle radius. The dimensionless particle radius is defined as follows:

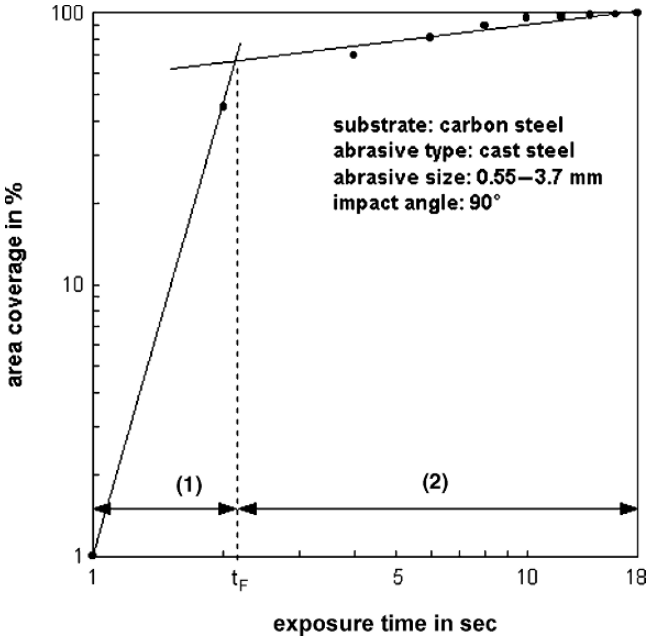

Fig. 3.36 Relationship between exposure time and area coverage (Tosha and Iida, 2001)

$$r_P^* = \frac{\dot{N}_P \cdot r_P}{v_P} \tag{3.43}$$

It is the number of particles launched in the time taken for a particle of average velocity to travel a distance equal to the particle radius. The dimensionless stand-off distance is defined as follows:

$$x^* = \frac{\dot{N}_P \cdot x}{v_P} \tag{3.44}$$

It is the number of particles launched in the time taken for a particle of average velocity to travel a distance equal to the stand-off distance between nozzle exit and target surface. The stream density can be applied to the calculation of a relative distance between abrasive particles as follows:

$$L_P^* = \frac{L_P}{d_P} = \left(\frac{\pi}{6 \cdot \rho_S^*}\right)^{1/3} \tag{3.45}$$

This parameter characterises the ratio between the average distance of two incident particles and the particle diameters.

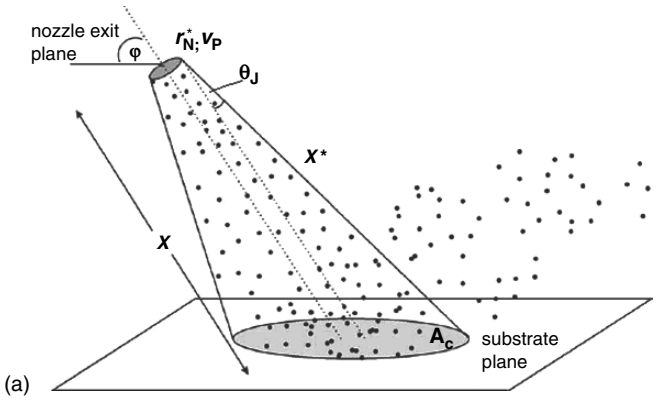

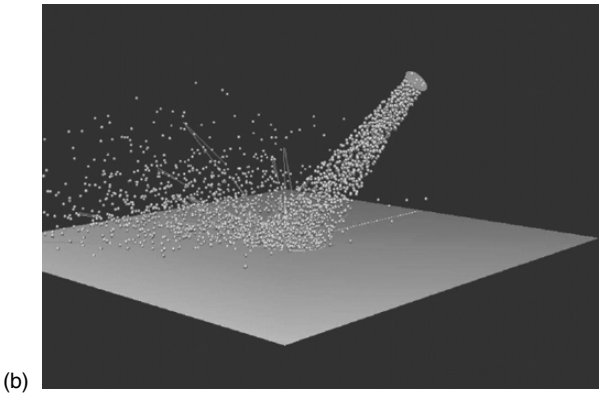

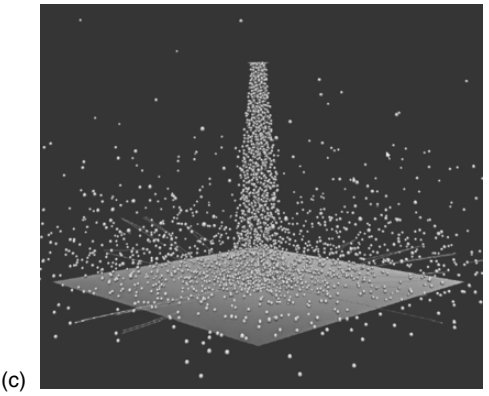

Fig. 3.37 Stream density (Ciampini et al., 2003a). (**a**) Geometric condition; (**b**) Simulation for oblique impact; (**c**) Simulation for normal impact

3.6 Parameter Effects on Abrasive Particle Velocity

3.6.1 Effects of Air Pressure on Particle Velocity

Tilghman (1870), in his original patent, wrote: "*The greater the pressure of the jet the bigger will be the velocity imparted to the grains of sand*." Generally, the relationship between air pressure and particle velocity can be described as follows:

$$v_P \propto p^{n_V} \tag{3.46}$$

The power exponent n_V seemed to depend on numerous process parameters, among them the abrasive mass flow rate. Some authors (Green et al., 1981; Lecoffre et al., 1993; Linnemann, 1997; Remmelts, 1969; Ruff and Ives, 1975) found a linear relationship between air pressure and abrasive particle velocity ($n_V = 1$). Remmelts (1969) reported that the coefficient of proportionality depended on abrasive type. It was high for slag material (low material density) and low for cut steel wire (high material density). Results delivered by Belloy et al. (2000), Clausen and Stangenberg (2002), Linnemann et al. (1996), Ninham and Hutchings (1983), Stevenson and Hutchings (1995) and Zinn et al. (2002), however, suggest a power exponent $n_V < 1$ for numerous abrasive materials (e.g. glass beads, steel shot and ceramic abrasives). A solution to (3.31) delivers $n_V = 0.68$. Achtsnick (2005) performed a regression of experimentally estimated aluminium oxide particle (mesh 360) velocities in a cylindrical nozzle, and he estimated a power exponent of $n_V = 0.52$. Results of numerical simulations and of measurements performed by Fokke (1999) are displayed in Figs. 3.38 and 3.39. The results plotted in Fig. 3.39 suggest a power exponent of $n_V = 0.6$. These rather large deviations in the values could be attributed to the effects of other process parameters, namely abrasive mass flow rate and nozzle design, but also to assumptions made for the calculation procedures. Figure 3.39 illustrates the effect of the abrasive particle size on the power exponent. There is only a marginal effect of the particle diameter on the power exponent.

A rise in air pressure increases air density as well as air flow velocity; both effects contribute to an increase in the drag force according to (3.27). Measurements performed by Bothen (2000) have shown the following (particle diameter between $d_P = 23$ and 53 µm): abrasive particle velocity increased by +35% if the air pressure rose from $p = 0.2$ to 0.4 MPa; if air pressure rose from $p = 0.4$ to 0.6 MPa, abrasive particle velocity increased by +25%.

3.6.2 Effects of Abrasive Mass Flow Rate on Particle Velocity

Experimental results have shown that abrasive particle velocity dropped with an increase in the abrasive mass flow rate (Pashatskii et al., 1970; Green et al., 1981;

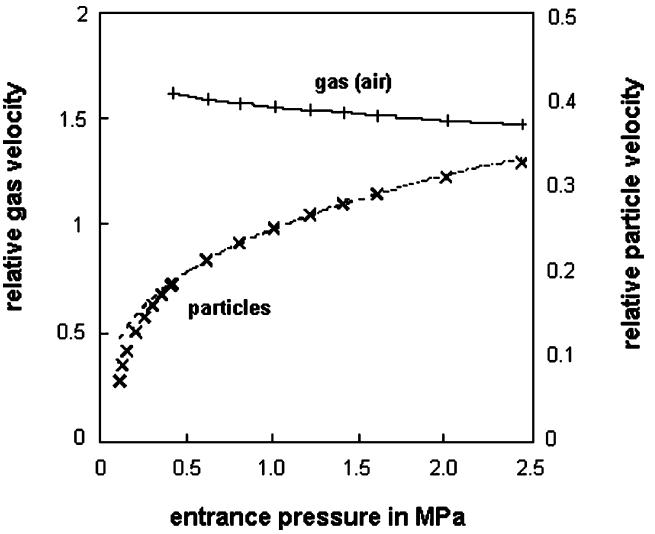

Fig. 3.38 Effect of air pressure on relative air velocity and relative particle velocity (Fokke, 1999). (Relative velocity is the ratio between actual velocity and velocity of sound.)

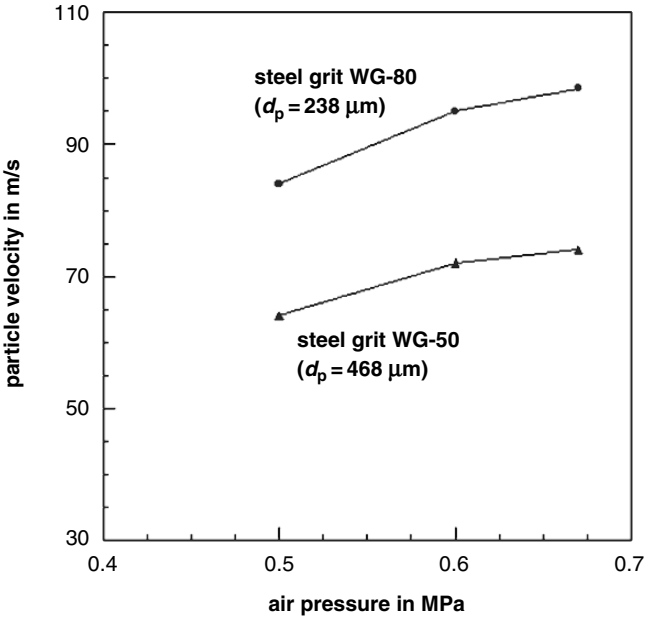

Fig. 3.39 Effects of air pressure and abrasive particle size on particle velocity (Fokke, 1999)

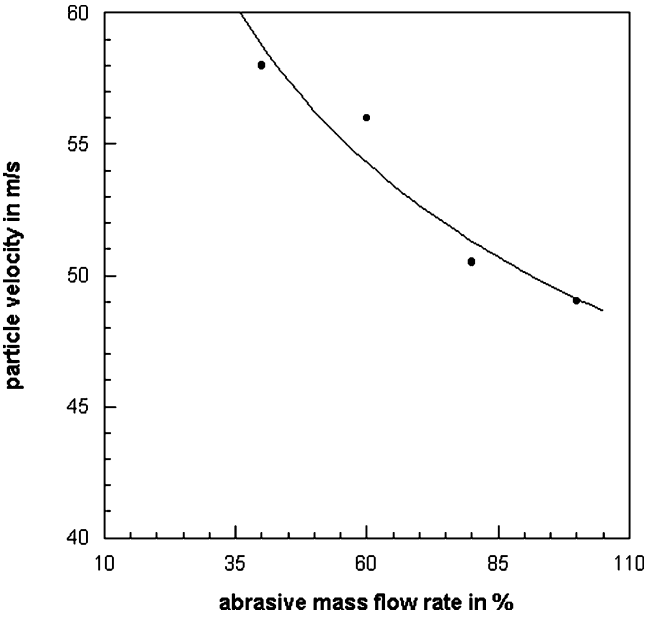

Fig. 3.40 Effect of relative abrasive mass flow rate on particle velocity (Lecoffre et al., 1993)

Lecoffre et al., 1993; Linnemann et al., 1996; Zinn et al., 2002). An example is shown in Fig. 3.40. The general trend is as follows:

$$v_P \propto \dot{m}_P^{-n_m} \tag{3.47}$$

The power exponent has values of $0 < n_m \leq 1$. If the impulse flow (respectively force) of the air flow according to (3.25) is considered, a value for the power exponent of $n_m = 1$ could be derived as a preliminary number.

Figure 3.41 shows the effects of changes in the mass flow ratio abrasive/air on the particle velocity. It can be seen that the particle velocity dropped if the mass flow ratio abrasive/air increased. This trend was observed by Hauke (1982), Pashatskii et al. (1970) and Wolak et al. (1977). The trend seemed to depend on the nozzle diameter for rather small R_m-values, and the influence of the nozzle diameter seemed to vanish for high values of R_m. Wolak et al. (1977) derived the following empirical relationship:

$$v_P \propto \exp(-k_R \cdot R_m) \tag{3.48}$$

Numerical simulations performed by Fokke (1999) for mass flow ratios up to $R_m = 6$ verified this trend: particle velocity dropped if mass flow ratio was increased. The author could also show that the effect of the mass flow ratio abrasive/air on particle velocity was largest for ratios between $R_m = 0.1$ and 3.0.

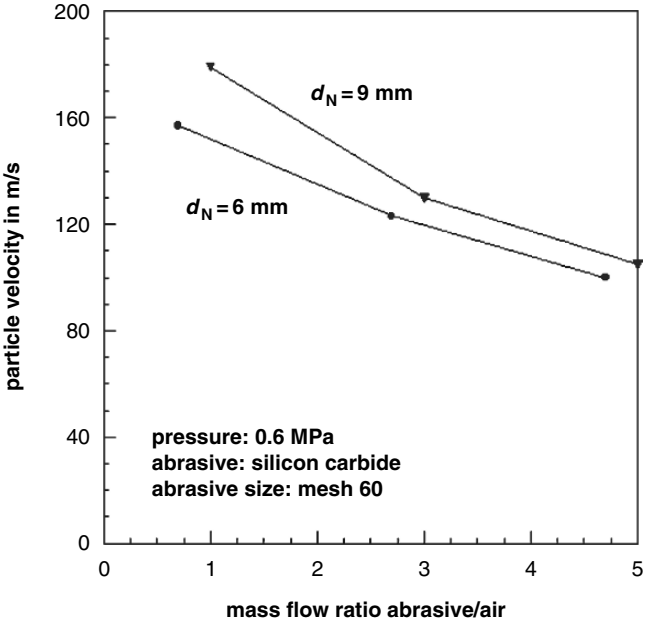

Fig. 3.41 Effects of mass flow ratio abrasive/air and nozzle diameter on particle velocity (Wolak et al., 1977)

3.6.3 Effects of Abrasive Particle Size on Particle Velocity

Measurements performed by several authors have shown that abrasive particle velocity dropped with an increase in the abrasive particle size. This trend was verified through experimental results provided by Achtsnick (2005), Fokke (1999), McPhee (2001), McPhee and Ebadian (1999), Neilson and Gilchrist (1968), Pashatskii et al. (1970), Stevenson and Hutchings (1995) and Zinn et al. (2002). Examples are shown in Fig. 3.39 and in Figs. 3.42–3.44. Achtsnick (2005) and Stevenson and Hutchings (1995) applied different nozzle types, and they measured particle velocities of particles in the diameter range between $d_P = 63$ and 500 µm. They derived the following regression function:

$$v_P \propto d_P^{-n_d} \tag{3.49}$$

The power exponent took a value of $n_d = 0.29$ for a cylindrical nozzle (Stevenson and Hutchings, 1995), and it took a value of $n_d = 0.36$ for a Laval nozzle with a square cross-section (Achtsnick, 2005). A solution to (3.31) delivers $n_d = 0.36$. Larger particles offer a larger projection area, which, according to (3.27), allows higher friction forces. However, due to their higher weight, larger particles need a longer acceleration distance to achieve a demanded final velocity according to (3.29). Fokke (1999) as well as Settles and Garg (1995) performed numerical

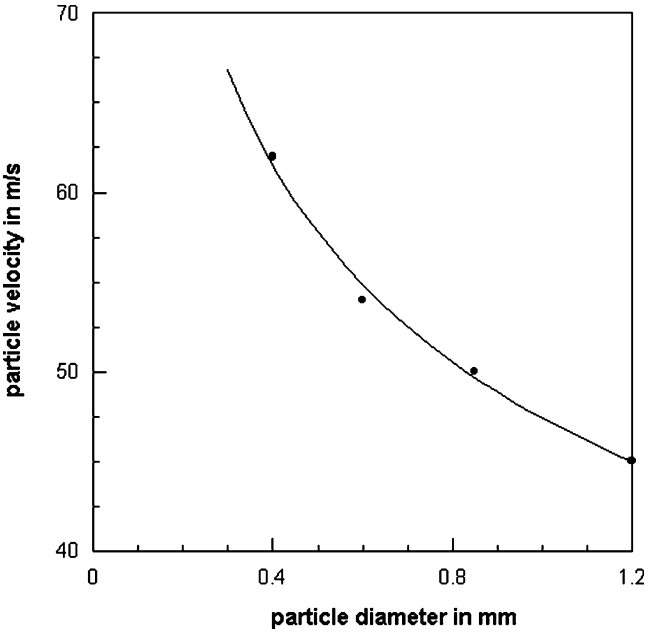

Fig. 3.42 Effect of abrasive particle diameter on particle velocity (Lecoffre et al., 1993)

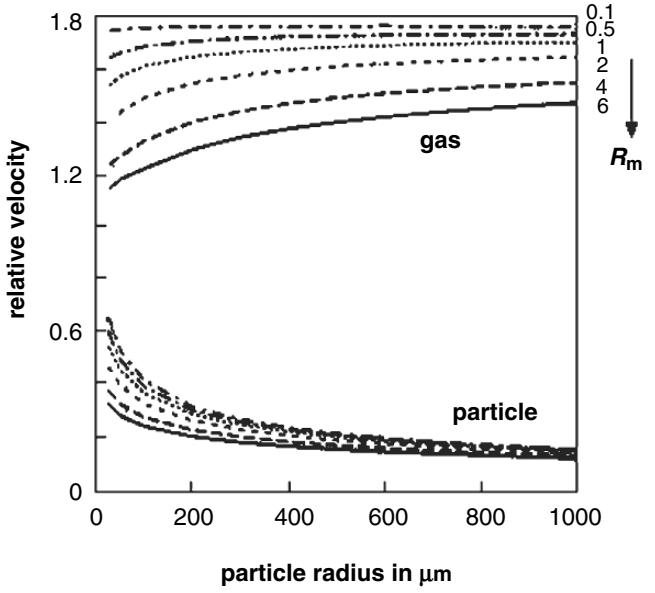

Fig. 3.43 Effects of abrasive particle diameter and mass flow ratio abrasive/air on relative particle velocity and relative air velocity (Fokke, 1999). (Relative velocity is the ratio between actual velocity and velocity of sound.)

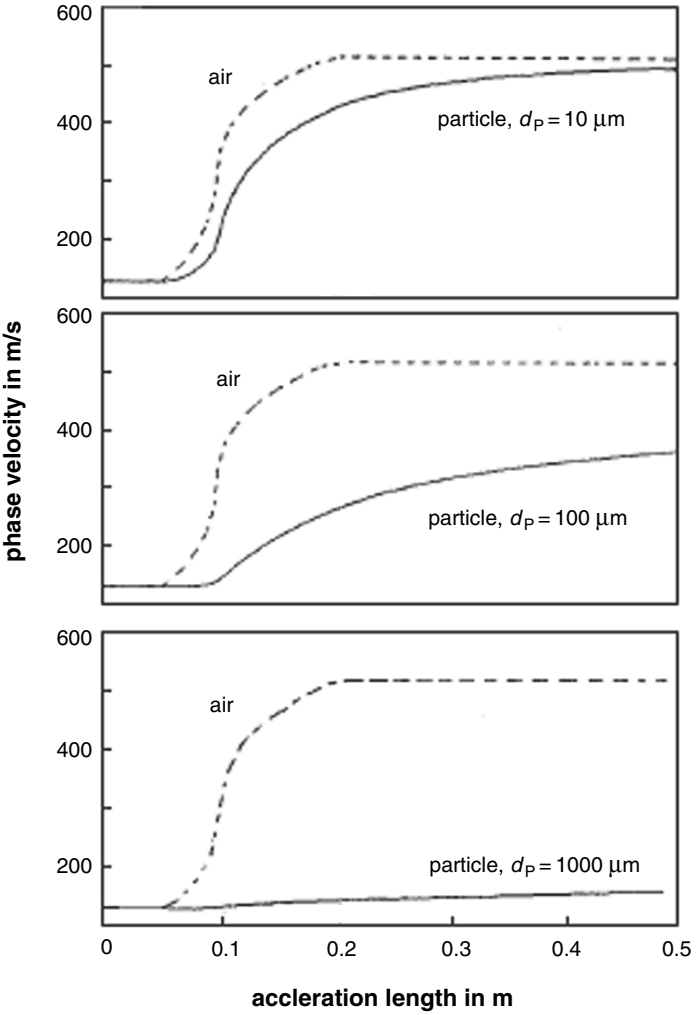

Fig. 3.44 Effect of abrasive particle diameter on particle velocity gradient in a convergent–divergent nozzle (Settles and Garg, 1995)

simulations for Laval-type nozzles, and they could prove that smaller abrasive particles could achieve higher velocities. Results of investigations are shown in Fig. 3.44. A particle with $d_P = 10$ µm reached a nozzle exit velocity of about $v_P = 500$ m/s, whereas a particle with a diameter of $d_P = 1{,}000$ µm reached a velocity of about $v_P = 150$ m/s only. The 10 µm particles lagged behind the airflow somewhat, but managed to achieve more than 80% of the air velocity at the nozzle exit. The 100 µm particles lagged more seriously and reached only about half the air velocity at the nozzle exit. The 1,000 µm particles were barely accelerated at all by the air flow in the nozzle. Settles and Garg (1995) performed measurements of the velocities

of steel particles (d_P = 50–70 µm) and aluminium particles (d_P = 50–70 µm) accelerated in convergent–divergent nozzles, and they found excellent agreement between the measured velocities and the velocities calculated with their simulation method. The gain in using smaller abrasive particles was especially evident for short nozzles. If longer nozzles were utilised, the influence of the abrasive particle diameter became less important.

3.6.4 Effects of Abrasive Particle Shape on Particle Velocity

A very early statement on the effect of the abrasive particle shape on the particle velocity, based on experimental results, was due to Rosenberger (1939): "*The shape of the abrasive particles also influences the velocity. Spherical particles travel slower than angular particles, other conditions being equal.*"

Shipway and Hutchings (1993a) found experimentally that glass spheres achieved lower final velocities than irregular silica particles for a given air pressure for many nozzle types. They attributed this effect for two reasons. Firstly, the irregularity of the silica shapes means that each particle with a given (sieve) diameter may have less mass than a sphere of this diameter, and may also have a greater drag coefficient. Secondly, the rebound behaviour of spheres and angular particles at the nozzle walls will differ. For a sphere, the rebound angle tended to be equal to or larger than the approach angle. An angular particle can rotate on impact, leading to a rebound angle which can be smaller than the approach angle. This may lead to higher acceleration along the nozzle, and therefore a greater final velocity. Fokke (1999) applied a numerical procedure developed for spherical steel particles and compared the numerical results with experimental results obtained with irregular steel grit particles. He noted a 20% difference between numerical and experimental results. This 20% increase in abrasive particle velocity for grit particles is, however, a very preliminary number, and further research is needed.

3.6.5 Effects of Abrasive Material Density on Particle Velocity

A very early statement on the effect of the abrasive material density on the particle velocity, based on experimental results, was due to Rosenberger (1939): "*The abrasive velocity bears some relation to the specific gravity of the abrasive material, being lowest when the specific gravity is high and vice versa.*"

Results from measurements performed by Stevenson and Hutchings (1995) with a cylindrical nozzle in the abrasive material density range between $\rho_P = 2{,}500\,\mathrm{kg/m^3}$ (glass beads) and $5{,}600\,\mathrm{kg/m^3}$ (zirconia sand), and investigations performed by Neilson and Gilchrist (1968a) and by Remmelts (1969) have shown that particle velocity dropped if particle material density increased. An empirical relationship reads as follows:

$$v_P \propto \rho_P^{-n_\rho} \tag{3.50}$$

Stevenson and Hutchings (1995) estimated a value of $n_\rho = 0.54$. A solution to (3.31) delivers $n_\rho = 0.39$. This inverse relationship is basically due to the larger momentum of the heavier abrasive material, which, for equal particle diameter, requires longer acceleration distances. For longer nozzles, the difference in the terminal velocity will therefore reduce. Remmelts (1969) reported a velocity ratio of 1.45 for the velocities of crushed slag ($\rho_P = 2{,}900\,\mathrm{kg/m^3}$) and cut steel wire ($\rho_P = 7{,}800\,\mathrm{kg/m^3}$), which agrees well with the values plotted in Fig. 3.19.

If (3.50) is combined with (3.49), an *abrasive parameter* could be defined for cylindrical nozzles, which determines the effects of abrasive material parameters on the abrasive particle velocity:

$$v_P \propto \underbrace{d_P^{-n_d} \cdot \rho_P^{-n_\rho}}_{\text{abrasive parameter}} \tag{3.51}$$

Heavier particles (e.g. with higher density and larger diameter) would need a longer acceleration distance compared with lighter particles; the relationship is $a_P \propto (d_P \cdot \rho_P)^{-1}$ from (3.29). For a given acceleration distance, particle speed will, therefore, be lower for a heavy particle. This simple argument can partly explain the effects of particle diameter and particle material density.

3.6.6 Effects of Stand-off Distance on Particle Velocity

Bothen (2000), Fokke (1999), Uferer (1992) and Wolak et al. (1977) performed studies into the effects of the stand-off distance on the velocity of abrasive particles. Results of these studies are displayed in Figs. 3.45–3.47. Figure 3.39 shows the effect of variations in stand-off distance on the relative abrasive particle velocity. It was evident that an optimum stand-off distance existed where abrasive particle velocity had maximum values. Because there is still a velocity slip between particles and accelerating gas if the flow exits the nozzle, the particles will be further accelerated until gas and solid medium flow at equal velocities. This effect, illustrated in Fig. 3.46 for two different nozzle types and two different abrasive materials, was experimentally verified by high-speed photograph inspections performed by Bothen (2000). A velocity balance will occur at a certain critical distance from the nozzle exit. If this stand-off distance is being exceeded, particle velocity will start to drop due to effects of air friction. The graphs in Fig. 3.47 illustrate the effect of mass flow ratio abrasive/air on the abrasive velocity. It can be seen that a stand-off distance effect was rather pronounced for the lowest mass flow ratio (the highest air mass flow value). It also seemed from these results that the optimum stand-off distances shifted to higher values for higher mass flow ratios abrasive/air (lower air mass flow rate).

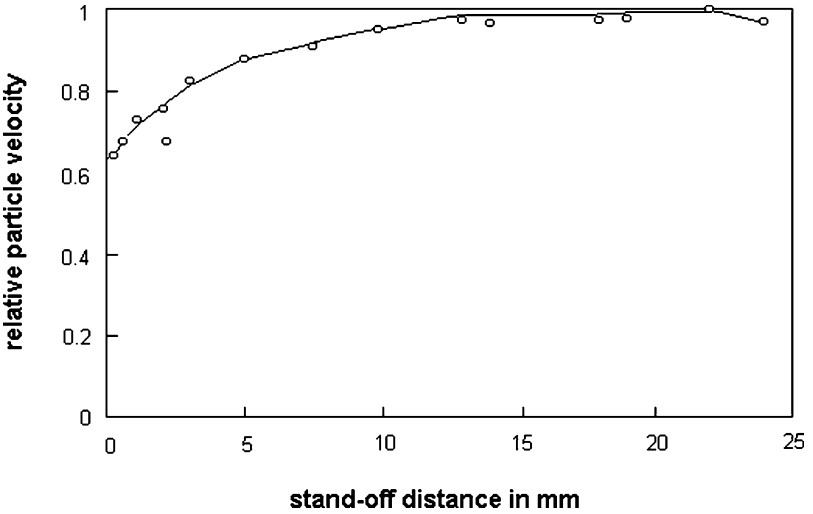

Fig. 3.45 Effect of stand-off distance on relative particle velocity (Bothen, 2000). (Relative velocity is related to the value "1", which characterises the maximum particle velocity.)

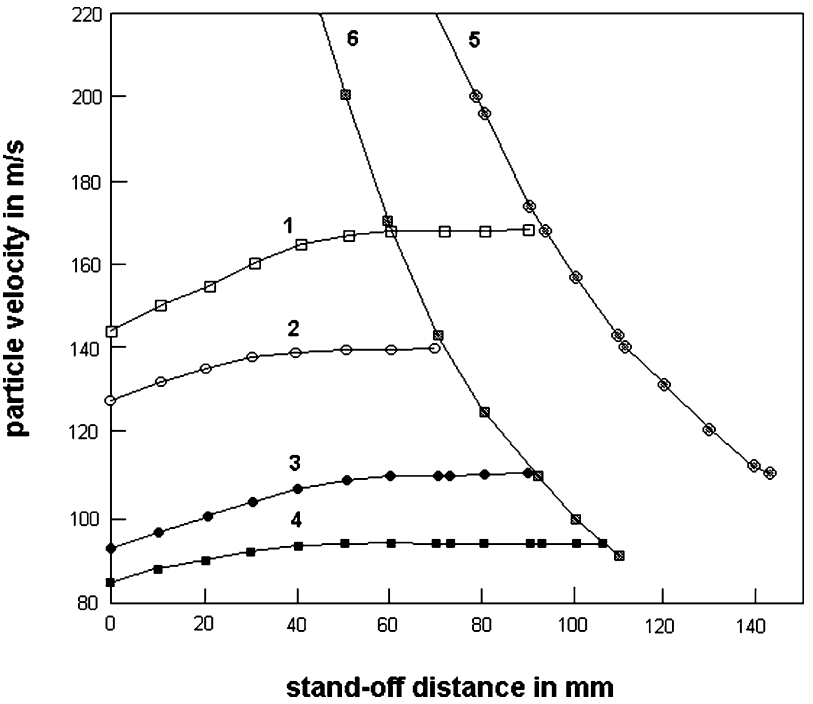

Fig. 3.46 Effect of stand-off distance on particle velocity (Uferer, 1992). "1" – convergent–divergent nozzle (slag); "2" – cylindrical nozzle (slag); "3" – convergent–divergent nozzle (steel cut wire); "4" – cylindrical nozzle (steel cut wire); "5" – convergent–divergent nozzle (air flow only); "6" – cylindrical nozzle (air flow only)

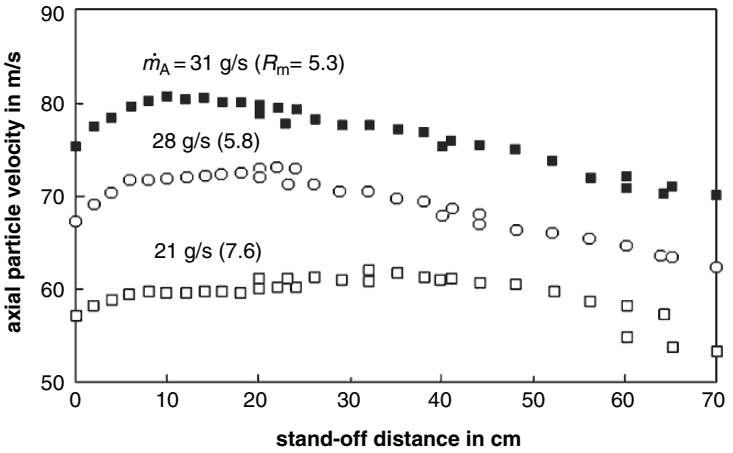

Fig. 3.47 Effects of stand-off distance and air mass flow rate (respectively mass flow ratio abrasive/air) on particle velocity (Fokke, 1999); $d_P = 468$ µm

3.6.7 Effects of Nozzle Length and Nozzle Diameter on Particle Velocity

Results of measurements on the effect of nozzle length on abrasive particle velocity are illustrated in Fig. 3.48. It can be seen that optimum nozzle lengths existed where velocity was highest (Wolak et al., 1977; Stevenson and Hutchings, 1995). This optimum slightly shifted to smaller nozzle length values if nozzle diameter decreased, but it did not seem to depend on the mass flow rate abrasive/air. The nozzle length to give the maximum axial particle velocity, at any given mass flow ratio, was approximately equal to 20 internal diameters of the nozzle for a cylindrical nozzle (Wolak et al., 1977). The dependence of particle velocity on nozzle length, and especially the existence of an optimum nozzle length, may be attributed to several mechanisms. Increased nozzle length increases the time during which the particles are exposed to the acceleration by the air, and consequently the particle velocities increase. However, a longer nozzle imposes proportionally higher friction effects on the air flow, and air velocity and the drag on the particle would decrease resulting in lower particle velocities. Another factor is the friction between particles and nozzle wall, evidenced through the wear of the nozzle walls. This expenditure of particle energy will also reduce particle velocities.

Abrasive particle velocity increased if nozzle diameter increased; this is shown in Figs. 3.41 and 3.48. However, it can be seen from Fig. 3.41 that this effect seemed to vanish for higher values of the mass flow ratio abrasive/air and for short nozzles.

3.6.8 Effects of Nozzle Design on Particle Velocity

Figure 3.49 displays results of abrasive particle measurements performed by Hamann (1987) on blast cleaning nozzles with different layouts. It can be seen that the highest

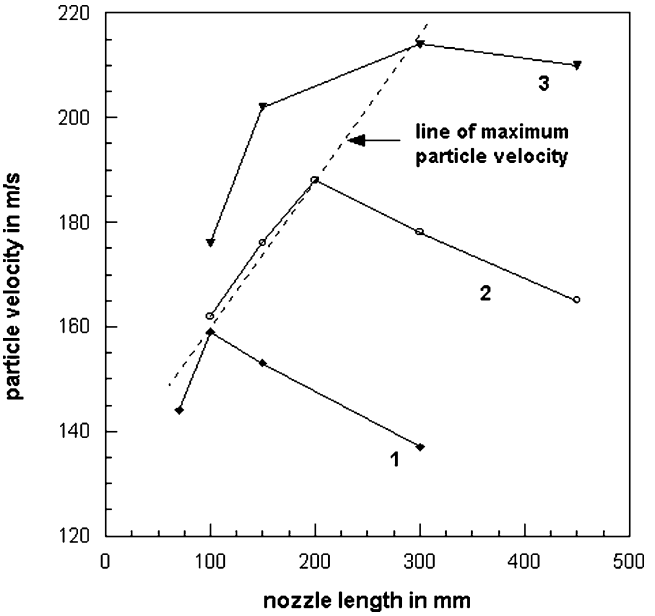

Fig. 3.48 Effects of nozzle length, nozzle diameter and mass flow ratio abrasive/air on particle velocity (Wolak et al., 1977); abrasive type: silicone carbide (mesh 60). "1" – $d_N = 6$ mm, $0.75 < R_m < 1.30$; "2" – $d_N = 9$ mm, $0.88 < R_m < 1.33$; "3" – $d_N = 12$ mm, $0.45 < R_m < 0.71$

abrasive particle velocity could be realised with a divergent–convergent nozzle with a specially designed inlet flow section (nozzle type "4"). The lowest abrasive particle velocity was delivered by a cylindrical nozzle with a bell-shaped inlet section (nozzle type "1"). The differences in abrasive particle velocities were as high as 45% among the tested nozzle layouts. Figure 3.50 shows the effects of the cross-section geometry on the velocity of abrasive particles. It can be recognised that the utilisation of a rectangular cross-section could notably increase the particle velocity compared with the use of a conventional circular cross-section. The effect of the nozzle cross-section on the abrasive particle velocity depended on the nozzle air pressure. The increase in abrasive particle velocity was +67% for a nozzle pressure of $p = 0.45$ MPa, and it was +93% for a nozzle pressure of $p = 0.57$ MPa.

3.6.9 Effects of Nozzle Wall Roughness on Particle Velocity

Shipway and Hutchings (1993a) could prove that the velocities of glass beads accelerated in cylindrical stainless steel nozzles depended on the roughness of the inner nozzle wall. The smoother the wall surface, the higher were the exit velocities of the particles. For a pressure of $p = 0.06$ MPa, for example, the theoretical particle velocity for glass beads ($d_P = 125$–150 µm) was $v_P = 100$ m/s; the particle velocity measured with a smooth nozzle ($R_a = 0.25$ µm) was $v_P = 85$ m/s and the particle

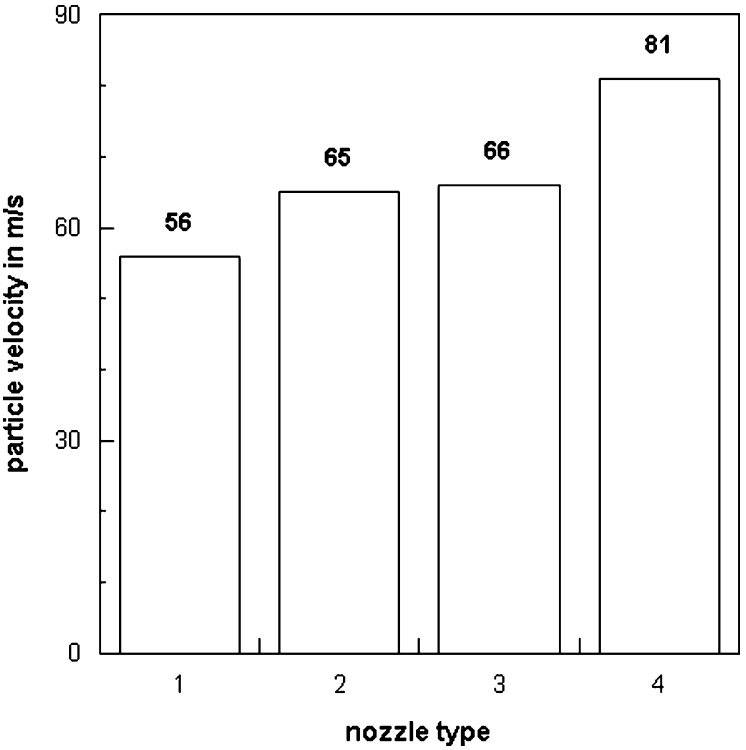

Fig. 3.49 Effects of nozzle type on abrasive particle velocity (Hamann, 1987). Nozzle type: "1" – bell-mouthed + cylinder; "2" – bell-mouthed + convergent; "3" – standard convergent–divergent; "4" – convergent–divergent with specially designed entry section

velocity measured with a rough nozzle ($R_a = 0.94\,\mu m$) was $v_P = 65$ m/s only. It was also shown that the standard deviation for the particle exit velocity increased with an increase in wall roughness. These results were attributed to rebound effects. As the wall roughness increases, the rebound angle tended to increase, leading to a shorter distance between successive impingement points along the nozzle. The impact of abrasive particles with the nozzle wall can be assumed to be a stochastic event, with some particles impacting many times, and others rarely. There will thus be a spread of particle exit velocities, which will tend to increase with wall roughness.

3.6.10 Scaling Laws for Abrasive Particle Velocity

Shipway and Hutchings (1995) performed an extensive experimental study in order to investigate the effect of process parameters on the velocity of abrasive particles accelerated in a cylindrical nozzle. Some results of this study are already presented in Fig. 3.32. Abrasive materials considered in their study included silica sand ($d_P = 90$–$710\,\mu m$; $\rho_P = 2{,}650\,kg/m^3$), soda lime glass ballotini ($d_P = 125$–$150\,\mu m$;

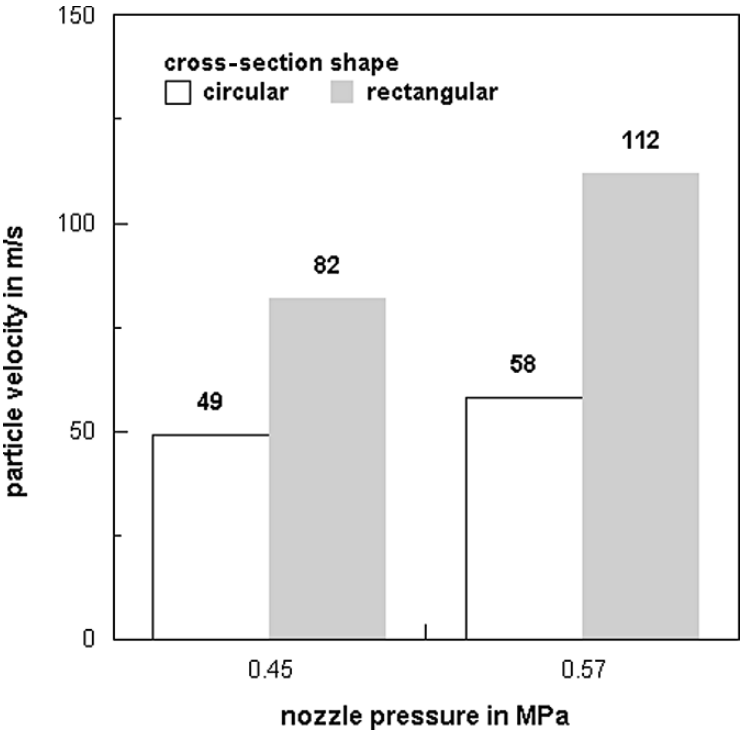

Fig. 3.50 Effects of pressure and nozzle cross-section shape on the velocity of abrasive particles (McPhee et al., 2000)

$\rho_P = 2{,}500\,kg/m^3$), aluminium oxide ($d_P = 63$–$75\ \mu m$; $\rho_P = 3{,}950\,kg/m^3$), silicon carbide ($d_P = 125$–$150\ \mu m$; $\rho_P = 3{,}160\,kg/m^3$), steel shot ($d_P = 212$–$300\ \mu m$; $\rho_P = 7{,}980\,kg/m^3$) and zirconia sand ($d_P = 125$–$500\ \mu m$; $\rho_P = 5{,}600\,kg/m^3$). The authors summarised their results with the following regression equation:

$$v_P \propto \left(\frac{p}{d_P^{0.57} \cdot \rho_P^{1.08}} \right)^{0.5} \tag{3.52}$$

The scaling law for the estimation of the ratio between air velocity and abrasive particle velocity had the following form:

$$\frac{v_P}{v_A} \propto d_P^{-0.285} \cdot \rho_P^{-0.54} \tag{3.53}$$

Both scaling laws are valid for parallel-sided cylindrical nozzles with a nozzle diameter of about $d_N = 5$ mm and for rather low nozzle pressures between $p = 0.005$ and 0.035 MPa.

3.7 Abrasive Stream Energy Flow and Nozzle Efficiency

The energy flow of an abrasive stream exiting a blast cleaning nozzle is given through the following relationship:

$$\dot{E}_P = \frac{1}{2} \cdot \dot{m}_P \cdot v_P^2 \tag{3.54}$$

This relationship is equal to (2.15). The energy flow can be estimated if abrasive particle velocity and abrasive mass flow rate can be measured. Results plotted in Fig. 3.51 illustrate that the abrasive stream energy flow (exit stream power) depended on nozzle design. A convergent–divergent nozzle with a specially designed entry flow section delivered a value of about $\dot{E}_P = 500$ Nm/s, whereas a cylindrical nozzle with a bell-mouthed inlet section delivered a value of $\dot{E}_P = 209$ Nm/s only. This is a difference of about 240%. If the abrasive stream energy flow is related to the power of the compressor consumed for the compression of the air (see Sect. 4.2.2), an efficiency parameter can be derived as follows:

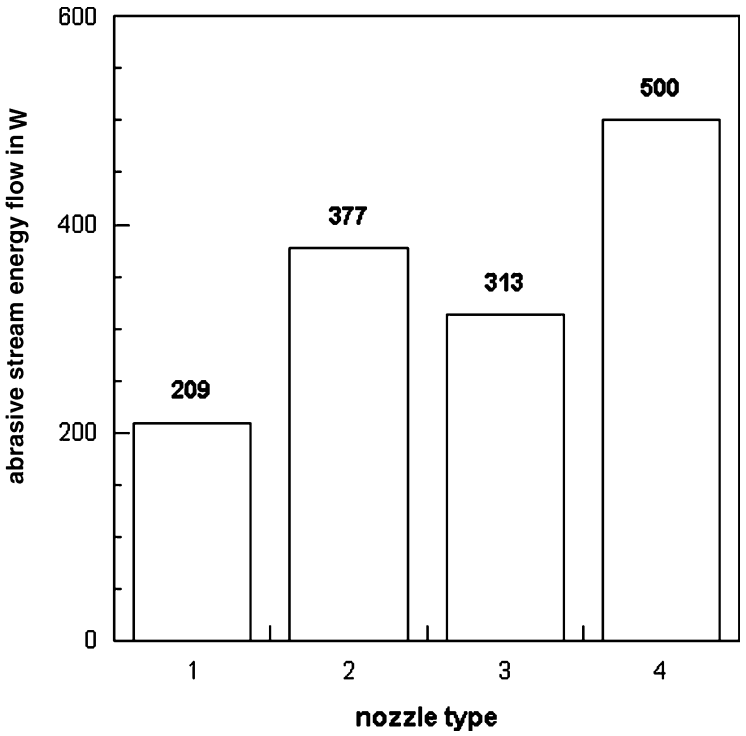

Fig. 3.51 Effects of nozzle type on abrasive stream energy flow (Hamann, 1987). Nozzle type: "1" – bell-mouthed + cylinder; "2" – bell-mouthed + convergent; "3" – standard convergent–divergent; "4" – convergent–divergent with specially designed entry section

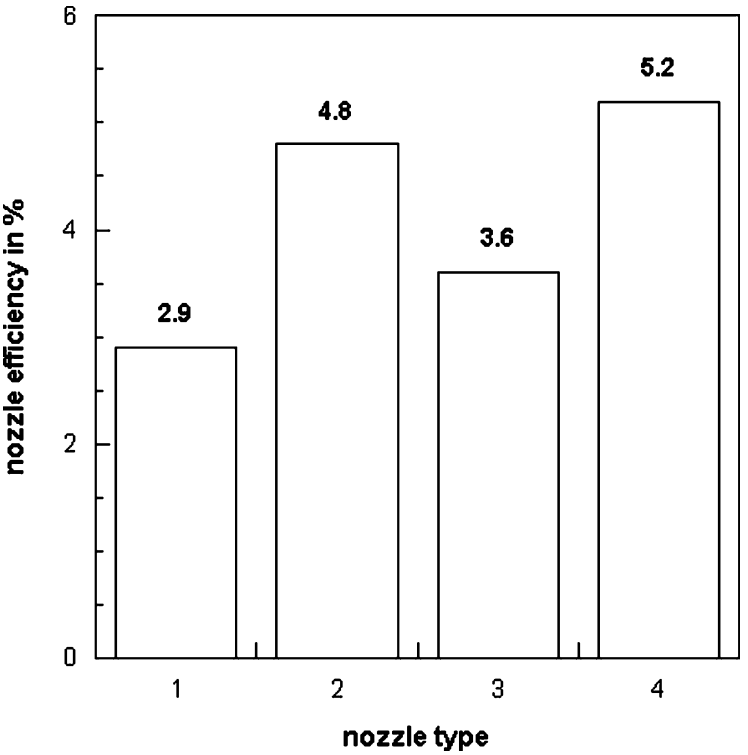

Fig. 3.52 Effects of nozzle type on efficiency (Hamann, 1987). Nozzle type: "1" – bell-mouthed + cylinder; "2" – bell-mouthed + convergent; "3" – standard convergent–divergent; "4" – convergent–divergent with specially designed entry section

$$\eta_N = \frac{\dot{m}_P \cdot v_P^2}{2 \cdot P_H} \tag{3.55}$$

This parameter describes the power transfer between compressed air and abrasive particles. The higher this efficiency parameter, the better is the power transfer. Results of measurements on the effects of varying nozzle types are displayed in Fig. 3.52. The trend is equal to that shown in Fig. 3.51. The certain values are between $\eta_N = 3$ and 5%. Similar results were reported by Uferer (1992). If the compressor power (P_H) in (3.49) is replaced by the power available at the nozzle inlet, (3.55) can characterise the quality of blast cleaning nozzles. According to this criterion, the nozzle with the best quality would be nozzle "4" in Fig. 3.52.